Published in final edited form as:

Cell Rep. 2021 February 23; 34(8): 108774. doi:10.1016/j.celrep.2021.108774.

Cell-type-specific recruitment of GABAergic interneurons in the primary somatosensory cortex by long-range inputs

Shovan Naskar[1], **Jia Qi**[1], **Francisco Pereira**[2], **Charles R. Gerfen**[3], **Soohyun Lee**[1,4,*]

[1]Unit on Functional Neural Circuits, National Institutes of Health, Bethesda, MD 20892, USA

[2]Machine Learning Team, National Institutes of Health, Bethesda, MD 20892, USA

[3]Section on Neuroanatomy, National Institute of Mental Health, National Institutes of Health, Bethesda, MD 20892, USA

[4]Lead contact

SUMMARY

Extensive hierarchical yet highly reciprocal interactions among cortical areas are fundamental for information processing. However, connectivity rules governing the specificity of such corticocortical connections, and top-down feedback projections in particular, are poorly understood. We analyze synaptic strength from functionally relevant brain areas to diverse neuronal types in the primary somatosensory cortex (S1). Long-range projections from different areas preferentially engage specific sets of GABAergic neurons in S1. Projections from other somatosensory cortices strongly recruit parvalbumin (PV)-positive GABAergic neurons and lead to PV neuron-mediated feedforward inhibition of pyramidal neurons in S1. In contrast, inputs from whisker-related primary motor cortex are biased to vasoactive intestinal peptide (VIP)-positive GABAergic neurons and potentially result in VIP neuron-mediated disinhibition. Regardless of the input areas, somatostatin-positive neurons receive relatively weak long-range inputs. Computational analyses suggest that a characteristic combination of synaptic inputs to different GABAergic IN types in S1 represents a specific long-range input area.

Graphical Abstract

*Correspondence: soohyun.lee@nih.gov.

AUTHOR CONTRIBUTIONS

S.N. and S.L. designed the study. S.N. and S.L. performed electrophysiology recording and data analysis. F.P. conducted computational modeling. J.Q. and C.R.G. performed and analyzed anatomical experiments. S.N. and S.L. wrote the manuscript.

DECLARATION OF INTERESTS

The authors declare no competing interests.

SUPPLEMENTAL INFORMATION

Supplemental information can be found online at https://doi.org/10.1016/j.celrep.2021.108774.

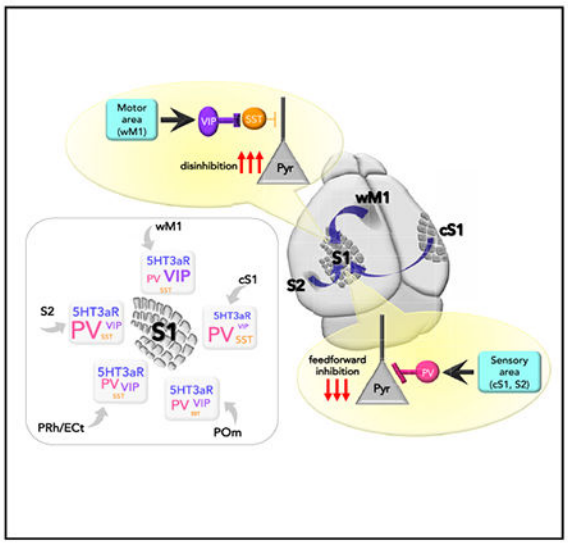

In brief

Naskar et al. show how functionally relevant brain areas interact with neurons in the primary somatosensory cortex, demonstrating that long-range projections from diverse brain areas differentially recruit specific subtypes of GABAergic neurons in S1, and each distinct subtype of GABAergic neurons differentially affects local network activity in S1.

INTRODUCTION

The mammalian neocortex is divided into specialized areas that are dedicated to performing specific functions. However, these areas do not operate in isolation. Rather, they function together, in a concerted manner with other areas through long-range projections, thereby enabling complex cortical functions. Primary sensory cortices contain an extensive network of feedback projections from higher order brain regions in addition to feedforward pathways (Hooks, 2017; Oh et al., 2014; Van Essen et al., 1992; Zingg et al., 2014). These projections convey behaviorally relevant information to primary sensory cortex for context-dependent sensory processing (Abs et al., 2018; Batista-Brito et al., 2018; Chen et al., 2013; Gentet et al., 2012; Gilbert and Li, 2013; Khan and Hofer, 2018; Larkum, 2013; Letzkus et al., 2011; Manita et al., 2015; Meyer, 2011; Zhang et al., 2014). The mechanisms by which sensory information is propagated from periphery to cortex through feedforward pathways are relatively well understood. However, despite the importance often attributed to long-range communication in the brain, the connectivity rules governing circuit specificity of long-range connections remain unclear (Marques et al., 2018; Petreanu et al., 2009; Turi et al., 2019).

Although GABAergic neurons in cortex constitute only a small portion of total cortical neurons, they comprise a remarkable array of unique subtypes (Bakken et al., 2018; Fishell and Kepecs, 2019; Pelkey et al., 2017; Tasic et al., 2016; Tremblay et al., 2016). Diversity in cortical GABAergic interneurons (INs) is considered to increase the capacity of cortical computation (Fishell and Kepecs, 2019; Pelkey et al., 2017; Tremblay et al., 2016). For

example, distinct cohorts of GABAergic INs are differentially engaged in context-dependent manners during behavior (Chen et al., 2013; Dipoppa et al., 2018; Gentet et al., 2012; Kuchibhotla et al., 2017; Kvitsiani et al., 2013; Lee et al., 2019; Letzkus et al., 2011; Muñoz et al., 2017; Palmer et al., 2012; Schneider et al., 2014; Turi et al., 2019; Xu et al., 2019). A vasoactive intestinal peptide (VIP) IN-mediated disinhibitory circuit motif has emerged as a critical feature for long-range corticocortical and top-down feedback connections across multiple cortical areas and hippocampus (Chamberland and Topolnik, 2012; Chen et al., 2013; Kuchibhotla et al., 2017; Lee et al., 2013; Pfeffer et al., 2013; Pi et al., 2013; Turi et al., 2019; Zhang et al., 2014). VIP INs preferentially inhibit other GABAergic INs, in particular, dendrite-targeting somatostatin (SST) INs, thereby disinhibiting local pyramidal (Pyr) neurons (Chen et al., 2013; Karnani et al., 2016; Pfeffer et al., 2013). The main inputs to VIP INs are glutamatergic excitatory inputs from higher order cortical areas (Lee et al., 2013; Zhang et al., 2014) and neuromodulatory inputs from subcortical areas (Alitto and Dan, 2013; Fu et al., 2014). Because of the identity of these input sources, it has been suggested that disinhibition mediated by VIP INs plays an important role in top-down signaling of context- and brain state-dependent behavior (Batista-Brito et al., 2018; Hangya et al., 2014). Perturbation of VIP INs during development significantly disrupts cortical activity, leading to an impairment of sensory perception (Batista-Brito et al., 2017). However, to what extent VIP IN-mediated disinhibition is a canonical circuit motif engaged in cortical long-range projections to primary sensory cortex has not been systematically described.

Any given cortical area receives feedback projections from multiple brain areas. However, if VIP IN-mediated disinhibition serves as a canonical circuit motif for cortical long-range projections to primary sensory cortex, with the majority of long-range projections converging on VIP INs and engaging local networks, it raises an important issue: how can diverse long-range inputs be differentiated in S1? Alternatively, diverse long-range inputs may recruit different types of GABAergic INs as a means of parsing different inputs sources.

We investigated how multiple streams of information from diverse brain areas are functionally and anatomically organized in their communication to primary somatosensory cortex (S1). We hypothesized that long-range projections from divergent cortical areas might differentially recruit specific subtypes of GABAergic neurons in S1 and that, in turn, each distinct subset of GABAergic neurons might differentially sculpt local microcircuit activity. We first identified the brain areas that project to the supragranular layers of S1 using retrograde viral tracing methods. On the basis of this anatomical study, we investigated the functional connectivity from these major input areas to the different neuronal types in the supragranular layers of S1 using optogenetics and whole-cell patch-clamp recordings in *ex vivo* preparations. In contrast to engagement of VIP IN-mediated disinhibition by whisker-related primary motor cortex (wM1) to S1 projections, we found that long-range projections from different areas preferentially engage distinct sets of GABAergic neurons in the supragranular layers of S1. Projections from secondary somatosensory cortex (S2) and contralateral S1 (cS1) strongly recruit parvalbumin (PV)-positive neurons. SST neurons received relatively weak long-range inputs regardless of input area. We further demonstrate that sensory-related information is transmitted to S1 by engaging PV IN-mediated feedforward inhibition, while motor-related information propagates to S1 through VIP IN-

mediated disinhibition. Together, our results suggest that primary sensory cortex may differentiate information from diverse long-range projections by means of input area-dependent, preferential recruitment of specific types of GABAergic INs.

RESULTS

Whole-brain mapping of diverse long-range inputs to S1

We first identified brain areas that project to the supragranular layers of S1 using retrograde viral tracing methods. We used the recombinant adeno-associated virus (rAAV) 2-retro (Tervo et al., 2016) to deliver Cre recombinase to an Ai14 reporter mouse line (Ai14Rosa26-Lox-STOP-Lox-tdTomato) (Madisen et al., 2010). Because we were interested mostly in long-range interactions, we restricted the rAAV-retro-Cre injection specifically to the supragranular layers of S1. Three weeks after injection, whole brains were sectioned, imaged, and registered to the Allen Mouse Brain Common Coordinate Framework (Eastwood et al., 2019). Each input neuron defined by expression of tdTomato was assigned to a specific brain region according to the Allen Brain Atlas. Consistent with previous studies, a wide range of brain areas projected to the supragranular layers of S1 (Figure 1A) (Aronoff et al., 2010; DeNardo et al., 2015; Oh et al., 2014). As expected, most input areas were ipsilateral, with a few exceptions such as the perirhinal cortex (PRh) (percentage of cells ipsilateral versus contralateral, 0.51 ± 0.11 versus 0.67 ± 0.18) and retrohippocampal (RHP) regions (percentage of cells ipsilateral versus contralateral, 0.96 ± 0.16 versus 1.35 ± 0.30) (Figure 1B). On the basis of the results of our whole-brain analyses, we focused on five brain regions that showed abundant projections to the supragranular layers of S1. These areas included wM1, S2, cS1, ectorhinal cortex (ECt) and PRh, and the posteromedial nucleus of the thalamus (POm).

Laminar distribution of axons from other brain areas in S1

We confirmed axonal projections from the five brain areas to the supragranular layers of S1 and quantified their laminar distributions within S1 (Figures 1C and 1D). Although all five brain regions innervated the supragranular layers of S1, the innervation patterns throughout the cortical layers differed from each other. Axonal innervation from the frontal cortical area (wM1) and somatosensory-related secondary thalamic nucleus (POm) was strongly biased to the upper part of layer 1. In contrast, axons from sensory cortical areas (cS1 and S2) ramified throughout layer 2/3 and the lower part of layer 1 (Minamisawa et al., 2018). As described in previous studies, POm axons strongly innervated layer 5a in addition to the layer1 (Wimmer et al., 2010; Zhang and Bruno, 2019). We also found that the density of axons from S2 was increased in L5a (Figure 1D). Although multiple cortical and subcortical areas projected to S1 supragranular layers, the laminar innervation of their axons were differentially distributed.

GABAergic neurons are differentially recruited by diverse long-range inputs

Next, we investigated the functional connectivity from these diverse input areas to distinct neuronal subtypes in the supragranular layers of S1. We injected AAV vectors expressing ChR2 into different input areas around postnatal 28–30 days. We performed whole-cell patch-clamp recordings in *ex vivo* preparations to measure postsynaptic responses evoked by

photostimulation of ChR2-expressing axon terminals from diverse input areas. To access the vast majority of known neuronal subtypes in S1 supragranular layers, we used four transgenic mouse lines, PVCre;Ai9, SSTCre;Ai9, VIPCre;Ai9, and 5HT3aR.eGFP (Lee et al., 2010; Tremblay et al., 2016). As VIP INs are a subtype of 5HT3aR-postive INs, we crossed a VIPCre;Ai9 line with a 5HT3aR.eGFP line to differentiate VIP-negative INs and VIP-positive INs within the 5HT3aR IN subgroups. Hereafter, we use 5HT3aR INs to indicate non-VIP, 5HT3aR INs. Light-evoked synaptic responses were recorded from identified neurons. We recorded synaptic strengths from five different brain areas onto the four different types of GABAergic INs and to Pyr neurons in the supragranular layers of S1 (Figure S1). We included only neurons that exhibited light-evoked response with latency within 4 ms (Figure S1). To control the variability of ChR2 expression in different brain slices and among different mice, we performed simultaneous recordings from an identified IN and a nearby Pyr neuron. The peak amplitude of the first light-evoked excitatory postsynaptic currents (EPSCs) recorded from an identified GABAergic IN was normalized to the light-evoked first EPSC in the Pyr cell (Figures 2A–2E). This analysis provides a measurement of relative synaptic strength.

Consistent with a previous study (Lee et al., 2013), we found that excitatory inputs from wM1 strongly recruit VIP INs in S1. PV INs and Pyr neurons received similar amplitudes of excitatory input from wM1. SST INs receive significantly weaker inputs from wM1 (EPSCs normalized to Pyr; PV IN, 1.10 ± 0.15, 23 cells, six mice, $p = 0.3447$; VIP IN, 1.75 ± 0.31, 15 cells, seven mice, $p < 0.0001$; nonVIP-5HT3aR IN, 1.48 ± 0.36, 8 cells, three mice, $p = 0.3125$; SST IN, 0.49 ± 0.13, 11 cells, four mice, $p = 0.0244$; Wilcoxon signed-rank test; Figure 2A). We also recorded excitatory postsynaptic potentials (EPSPs) from different neuronal types. Photostimulation-evoked EPSP results were comparable with the EPSC results (Figure S2).

Next, we asked whether the patterns of synaptic connectivity from other brain areas to S1 were similar to those from wM1. In contrast to the strong synaptic connectivity from wM1 to VIP INs in S1, long-range projections from other brain areas provided different patterns of synaptic inputs to neurons in S1. The projections from S2 provided significantly stronger excitatory inputs to PV INs than to nearby Pyr neurons in S1, while S2 provided significantly weaker excitatory inputs to VIP INs (EPSCs normalized to Pyr; PV IN, 3.42 ± 0.85,15 cells, six mice, $p = 0.0034$; VIP IN, 0.93 ± 0.46, 13 cells, five mice, $p = 0.0105$; Wilcoxon signed-rank test; Figure 2B). To directly test monosynaptic responses, we also recorded the EPSCs from neurons evoked by photostimulation of wM1 and S2 inputs under the application of tetrodotoxin (TTX; 1 μM) and 4-aminopyridine (4-AP; 100 μM) (Petreanu et al., 2009) (Figure 3). The synaptic strength recorded in the presence of TTX and 4-AP were highly consistent with the results collected without the drugs (EPSCs normalized to Pyr, input areas, GABAergic INs, mean ± SEM, number of recorded neurons, number of mice used; S2, PV IN, 2.44 ± 0.33, 19, 3, $p < 0.0001$; VIP IN, 0.17 ± 0.04, 14, 3, $p = 0.0001$; non-VIP-5HT3aR IN, 0.23 ± 0.06, 14, 3, $p = 0.0001$; SST IN, 0.27 ± 0.11, 15, 3, $p = 0.0002$; wM1, PV IN, 0.78 ± 0.14, 19, 4, $p = 0.0071$; VIP IN,1.75 ± 0.29, 13, 4, $p = 0.0215$; non-VIP-5HT3aR IN, 0.65 ± 0.31, 13, 3, $p = 0.0171$; SST IN, 0.48 ± 0.09, 16, 3, $p = 0.0002$; Wilcoxon signed-rank test) (Figure 3). In current-clamp recordings, the strong recruitment of PV INs by S2 inputs often led to spikes from PV neurons (9 of 15 cells) but not from

nearby Pyr cells. Although S2 axons provided similar excitatory inputs to nonVIP-5HT3aR INs and Pyr cells in S1, SST INs received significantly weak inputs from S2 (EPSCs normalized to Pyr; nonVIP-5HT3aR IN, 1.46 ± 0.42, 6 cells, two mice, p = 0.6875; SST IN, 0.21 ± 0.09, 10 cells, five mice, p = 0.0020; Wilcoxon signed-rank test; Figure 2B).

Similar to the connectivity pattern from S2 to S1, the contralateral side of S1 (cS1) also provided significantly stronger excitatory inputs to PV INs than to nearby Pyr cells. In contrast to the connectivity from wM1 to S1, VIP INs in S1 received the least excitatory inputs from cS1 (EPSCs normalized to Pyr; PV IN, 2.44 ± 0.48, 13 cells, five mice, p = 0.0034; VIP IN, 0.28 ± 0.08, 12 cells, six mice, p = 0.0010; nonVIP-5HT3aR IN, 0.42 ± 0.12, 8 cells, four mice, p = 0.0156; SST IN, 0.55 ± 0.12, 10 cells, six mice, p = 0.0098; Wilcoxon signed-rank test; Figure 2C). Similar to S2 inputs, nearly half of the recorded PV INs (6 of 13 cells) elicited spikes in response to cS1 stimulation. ECt/PRh inputs did not exhibit preferential recruitment of any particular IN subtype over Pyr neurons, and provided significantly weaker input to SST INs (normalized to Pyr; PV IN, 1.38 ± 0.29, 9 cells, five mice, p = 0.7344; VIP IN, 0.80 ± 0.31, 7 cells, three mice, p = 0.3750; nonVIP-5HT3aR IN, 1.03 ± 0.47, 4 cells, three mice, p = 0.3750; SST IN, 0.40 ± 0.26, 11 cells, six mice, p = 0.0244; Wilcoxon signed-rank test; Figure 2D). Comparable with the pattern of ECt/PRh inputs to S1, POm inputs recruited most IN types similarly along with Pyr neurons in S1, except that SST INs and VIP INs received weaker inputs (EPSCs normalized to Pyr; PV IN, 1.34 ± 0.26, 10 cells, four mice, p = 0.4922; VIP IN, 0.51 ± 0.11, 13 cells, four mice, p = 0.0266; nonVIP-5HT3aR IN, 0.98 ± 0.39, 7 cells, five mice, p = 0.3750; SST IN, 0.09 ± 0.02, 16 cells, eight mice, p < 0.0001; Wilcoxon signed-rank test; Figure 2E). Recent studies of POm inputs to different types of cortical GABAergic neurons throughout different cortical layers are in agreement with our results (Audette et al., 2018; Sermet et al., 2019). To address whether the variability of individual Pyr neurons affect our results, we also normalized a GABAergic IN response to the averaged response of all recorded Pyr neurons per animal. The results from the averaged normalization analysis (Figure S3) were highly consistent with the previous results (Figure 2).

We compared whether Pyr cells in S1 received similar excitatory inputs from diverse brain areas, despite direct comparison of synaptic responses from different inputs could be misleading for several reasons, including differences in the coverage of the input areas with the viral injection. Excitatory inputs from wM1 were significantly stronger than those from S2, Pom, and ECt/PRh (S2 versus wM1, −121.53 ± 19.63 pA versus −191.78 ± 16.28 pA, p = 0.0041; POm versus wM1, −108.99 ± 11.82 pA versus −191.78 ± 16.28 pA, p = 0.0006; ECt/PRh versus wM1, −73.69 ± 10.68 pA versus −191.78 ± 16.28 pA, p < 0.0001) while excitatory inputs from ECt/PRh were significantly weaker than those from other brain areas, including cS1 and wM1 (ECt/PRh versus cS1, −73.69 ± 10.68 pA versus −166.63 ± 20.08 pA, p = 0.0009; ECt/PRh versus wM1, −73.69 ± 10.68 pA versus −191.78 ± 16.28 pA, p < 0.0001; one-Way ANOVA with post hoc Holm-Sidak multiple comparisons test; Figure S4). Taken together, our data suggest that long-range projections from relevant cortical areas recruit specific subtypes of GABAergic neurons in S1. Although projections from motor cortex strongly recruits VIP INs in S1, sensory cortices including S2 and cS1 provide significantly larger excitatory inputs to PV INs in the supragranular layers of S1. Unlike

other subtypes of GABAergic INs in S1, SST INs receive relatively weaker inputs from all long-range projections tested.

SST INs are weakly connected by long-range inputs

Our data suggest that different types of GABAergic INs receive input area-dependent, differential excitatory inputs from diverse brain regions, except SST INs. We observed that SST INs in the supragranular layers of S1, which are mostly L1-projecting, Martinotti-type SST INs (Kawaguchi and Kubota, 1997; Kubota, 2014; Ma et al., 2006; Muñoz et al., 2017; Naka et al., 2019; Wang et al., 2004; Xu et al., 2013), received significantly weaker long-range inputs, regardless of input area (Figure 2). Unlike most GABAergic INs and Pyr neurons, SST INs receive strongly facilitating excitatory inputs with high-frequency stimulation, regardless of the subtypes of SST INs (Beierlein et al., 2003; Kapfer et al., 2007; Naka et al., 2019; Nigro et al., 2018; Pouille and Scanziani, 2004; Silberberg and Markram, 2007; Xu et al., 2013). We wondered whether the relatively weak EPSCs recorded from SST INs was due to a low initial release probability that typically underlies the facilitating dynamics of excitatory synapses onto SST INs. To address this, we employed ChETA, one of the channelrhodopsin variants that has fast kinetics (Gunaydin et al., 2010). This allowed us to reliably apply high-frequency photostimulation (Figure 4A). Despite using high-frequency light stimulation (20 and 50 Hz, 10 pulses, 3 ms duration), long-range excitatory inputs only weakly recruited SST INs in S1, regardless of whether the inputs were from wM1 (tenth EPSC normalized to first EPSC; 10 Hz, 1.81 ± 0.52, $p = 0.1953$, 20 Hz, 1.32 ± 0.34, $p = 0.5781$; 50 Hz, 1.01 ± 0.26, seven cells, two mice, $p > 0.9999$; Wilcoxon signed-rank test) or S2 (tenth EPSC normalized to first EPSC; 10 Hz, 1.63 ± 0.39, $p = 0.2500$, 20 Hz, 1.75 ± 0.80, $p = 0.6250$; 50 Hz, 0.80 ± 0.34, four cells, three mice, $p = 0.6250$; Wilcoxon signed-rank test) (Figure 4B). Although long-range excitatory inputs from wM1 and S2 were not facilitating onto SST INs, these inputs did not show synaptic depression onto SST INs, while the same excitatory inputs exhibited strong synaptic depression in Pyr neurons (tenth EPSC normalized to first EPSC, 10 Hz; wM1, 0.65 ± 0.04, $p = 0.0078$; S2, 0.44 ± 0.06, $p = 0.0002$; Wilcoxon signed-rank test) (Figure 4B). Similar to Pyr cells, EPSCs recorded in PV, VIP, and non-VIP-5HT3aR INs depressed during repetitive photostimulation of diverse long-range inputs (Figure S5). This result suggests that SST INs in S1 are weakly connected by long-range inputs irrespective of input area, compared with other types of GABAergic INs.

S2-driven PV IN-mediated feedforward inhibition within S1

We next asked how the differential recruitment of specific sets of GABAergic neurons affect local network activity in the supragranular layers of S1. Our data suggest that sensory-related information from S2 and cS1 strongly engages PV INs, while motor-related information from wM1 dominantly recruits VIP INs in S1 (Figure 2). We hypothesized that inputs from sensory cortices, S2 and cS1, drive PV IN-mediated feedforward inhibition of Pyr neurons in S1. To directly test our hypothesis, we optogenetically inhibited PV INs while monitoring the S2-driven synaptic responses in S1 Pyr neurons (Figure 5A). Using a PV-Cre mouse line, we specifically expressed halorhodopsin (AAV5-EF1α-DIO-eNpHR3-mCherry) in S1 PV INs in a cre-dependent manner, while concomitantly expressing ChR2 (AAV5-hSyn-hChR2[H134R]-eYFP) in S2 neurons. Immunostaining confirmed that the

expression of NpHR3.0 was limited to PV INs (Figure 5B). We verified that the photoactivation of NpHR3.0 (590 nm) sufficiently hyperpolarized S1 PV INs such that the activation of S2 inputs was not able to elicit spikes from the PV Ins (Figures 5C). In current-clamp recordings, we slightly depolarized recorded Pyr neurons to be able to detect the effect of photoactivation on spike output. We alternated each recording sweep with and without application of photostimulation (590 nm) to suppress the activity of PV INs while photo-stimulating (470 nm) projections of S2 for every sweep. Pyr neurons in S1 supragranular layers significantly increased their spike probability in response to photostimulation of S2 axons when local PV INs were optogenetically inactivated (Figure 5D). We compared the number of spikes elicited in Pyr neurons with 470 nm only and with a combination of 470 and 590 nm photostimulation. Photo-inhibition of PV INs significantly increased spike output of Pyr neurons in S1 upon photostimulation of S2 inputs (470 + 590 nm spike counts normalized to 470 nm, 2.70 ± 0.81, 12 cells, five mice; $p = 0.0029$, Wilcoxon signed-rank test; Figure 5E).

To determine whether the PV IN-mediated feedforward inhibition was specific to S2 inputs, we repeated the same optogenetic manipulation to suppress PV INs, with the exception of photostimulation of wM1 axons instead of S2 axons. Although PV INs were strongly suppressed, the number of spikes elicited in S1 Pyr neurons by photostimulation of wM1 inputs was not changed (spike counts normalized to 470 nm, 1.12 ± 0.24, nine cells, three mice; $p > 0.9999$, Wilcoxon signed-rank test; Figure 5F). Together, these results suggest that PV INs mediate S2-driven feedforward inhibition onto Pyr neurons in S1, and that this PV IN-mediated feedforward inhibition is input area dependent.

wM1-driven VIP IN-mediated disinhibition within S1

Next, we investigated how projections from wM1 modulate the activity of S1 Pyr neurons. The functional connectivity of wM1 to different types of neurons in S1 has been described previously (Lee et al., 2013), and our present results support this earlier observation. The projections from wM1 strongly recruit VIP INs in S1 that, in turn, provide strong inhibition to SST INs, which target mostly the apical dendrites of Pyr neurons. *In vivo,* SST INs exhibit significantly decreased activity during whisking periods (Gentet et al., 2012; Muñoz et al., 2017). A similar circuit motif has been described in multiple cortical areas, including hippocampus (Adler et al., 2019; Cichon et al., 2017; Fu et al., 2014; Pfeffer et al., 2013; Pi et al., 2013; Turi et al., 2019; Zhang et al., 2014).

To test wM1-driven VIP IN-mediated disinhibition in an *ex vivo* preparation, we used optogenetic manipulation to suppress VIP INs while monitoring the wM1-driven synaptic response in S1 Pyr neurons. Similar to the strategy outlined above, we expressed halorhodopsin in VIP INs in S1 in a cre-dependent manner using a VIP-Cre mouse line, in combination with ChR2 expression in wM1 neurons (Figure 6A). Immunostaining confirmed that the expression of NpHR3.0 was limited to VIP INs (Figure 6B). Activation of NpHR significantly reduced wM1 activation-evoked spikes from NpHR-expressing VIP INs (Figure 6C). Because wM1-driven disinhibition is carried out by direct inhibition from VIP INs to SST INs, we used a modified artificial cerebrospinal fluid (ACSF) to induce spontaneous activity from SST INs. In this modified ACSF (see STAR methods) (Neske and

Connors, 2016), SST INs showed the most enhanced spontaneous spiking activity compared with VIP and PV INs (mean firing rate, SST INs, 5.92 ± 1.71 Hz, 7 cells, three mice; VIP INs, 1.18 ± 0.33 Hz, 12 cells, three mice; PV INs, 0.13 ± 0.12 Hz, 11 cells, three mice; Figure S6). Spontaneous firing rates of SST INs recorded in the modified ACSF were comparable with the spontaneous activity of SST INs in awake behaving animals (Gentet et al., 2012; Lee et al., 2013; Yu et al., 2019). Under this experimental condition, silencing VIP INs significantly reduced the activity of S1 Pyr neurons upon photostimulation of the projections from wM1. This is likely due to the lack of VIP IN-mediated inhibition of SST INs (spike counts normalized to 470 nm, 0.58 ± 0.09, 11 cells, five mice; $p = 0.0059$, Wilcoxon signed-rank test; Figure 6E).

To determine whether the VIP IN-mediated disinhibition was specific to wM1 inputs, we tested that silencing VIP INs affect the activity of S1 Pyr neurons to the photostimulation of S2 input. Inactivation of VIP INs did not affect the spiking activity of S1 Pyr neurons to the stimulation of S2 inputs (spike counts normalized to 470 nm, 1.03 ± 0.11, 10 cells, two mice; $p = 0.7813$, Wilcoxon signed-rank test; Figure 6F). Together these results demonstrate that VIP INs in the supragranular layers of S1 mediate disinhibition of Pyr neurons in S1 by directly inhibiting SST INs and that this disinhibition is specific to wM1 inputs.

Characteristic combination of long-range synaptic inputs to the different types of GABAergic INs in S1

Next, we asked whether the specific patterns of synaptic weights from different brain areas to four different types of GABAergic neurons in S1 are sufficiently different. To test this, we used a glmnet multinomial regression classifier, a supervised machine learning algorithm. We used the dataset in which photostimulation-evoked responses from individual GABAergic INs were normalized to the response from nearby Pyr neurons (Figures 2 and 7A). In brief, we used a fourfold cross-validation procedure. In each fold, the available data points for each combination of input areas and different types of GABAergic INs were partitioned into “training” or “testing” groups. Within each group, examples for each area were generated by taking every possible combination of data point from each of the four GABAergic IN types, yielding a dataset. Given that data points in training and testing groups were independent, the examples in training and testing sets were also independent. We used the training set to train the classifier and then applied the classifier to the test set, generating an input-area prediction for each example. We repeated this training and testing procedure for all four folds of the data, producing predicted input area label for each example and, from all of those, an average accuracy estimate, defined as the percentage of examples for which the prediction was correct. Given that this analysis relies on a stochastic process generating examples from data points, we repeated it 100 times, yielding 100 accuracy results and class confusion matrices. The average confusion matrix over 100 runs demonstrates that the classifier accurately predicted input source significantly higher than the chance level of 0.2 (average accuracy 0.43 ± 0.0016, 100 runs, 95% confidence interval; Figure 7B). The classifier predicted wM1, cS1, and S2 input with the highest accuracy, while it failed to predict ECt/PRh inputs (average accuracy: wM1, 0.46; cS1, 0.56; S2, 0.41; ECt/PRh, 0; POm 0.36). The classifier mis-predicted ECt/PRh inputs as either cS1 (0.43) or POm (0.41). This error of the classifier is likely due to the lack of cell-type-specific

recruitment of GABAergic INs (Figure 2D), thus the classifier placed little weight on any neuronal types (Figure S7).

To further address which types of GABAergic INs carry the most information to identify each input area, we repeated the training and testing procedure by excluding each type of GABAergic IN in turn (Figure S7). Without the information of synaptic strength onto PV INs, prediction accuracy of S2 was reduced close to the chance level. Similarly, prediction accuracy of wM1 was decreased when VIP INs were excluded. In contrast, elimination of SST INs from the training dataset minimally affected the performance of the classifier. The classification analysis revealed that a characteristic combination of synaptic inputs to the different types of GABAergic neurons better predicted the specific long-range input area, rather than the most strongly recruited single GABAergic IN type (Figures 7 and S7). Together, our computational data suggests that each long-range input area provides a distinct pattern of differential synaptic weights onto different IN types.

DISCUSSION

Here, we describe connectivity rules by which functionally relevant brain areas interact with diverse types of neurons in primary somatosensory cortex. On the basis of quantitative anatomical analysis of the whole brain, we selected five brain areas and investigated how these areas recruit different types of neurons in the supragranular layers of the somatosensory cortex. Projections from other whisker-related sensory cortices, secondary somatosensory cortex and the contralateral side of somatosensory cortex strongly recruit PV INs in S1, while inputs from primary motor cortex preferentially recruit VIP INs, as previously described (Lee et al., 2013). SST INs, dendritic targeting GABAergic INs, receive relatively weak inputs across multiple input areas. We further demonstrate that PV INs in S1 are responsible for S2-driven feedforward inhibition of Pyr neurons in S1. In contrast, we show that VIP INs are responsible for wM1-driven disinhibition of Pyr neurons in S1. Finally, using a machine learning classifier, our study suggests that each long-range input area provides a distinct set of cell-type-specific recruitment of GABAergic INs in the primary somatosensory cortex.

Functional implications of input area-dependent circuit motifs

Efficient sensory processing depends on active interactions among relevant brain areas. How does input area-dependent, preferential recruitment of specific types of GABAergic INs subserve *in vivo* dynamics of long-range communication during active sensory processing? Although our present study cannot directly address this question, as it was performed under *ex vivo* conditions, our study establishes comprehensive connectivity patterns for multiple input areas to different types of neurons in S1 supragranular layer. Our present findings provide a framework for computational models of long-range communication to primary sensory cortex.

Studies characterizing distinct activity profiles of different types of GABAergic INs in S1 during whisker-dependent sensory perception tasks suggest unique functional roles for each GABAergic IN type during active sensory processing (Sachidhanandam et al., 2016; Yu et al., 2019). These distinct functional properties of different types of GABAergic INs during

sensory processing can be explained by feedforward thalamocortical circuitry, and cortical intra- and interlaminar connectivity. Along with this feedforward processing, long-range corticocortical connectivity revealed in the present study expands our understanding of the circuit mechanisms underlying the response properties of each GABAergic IN subset during active sensing.

We assessed the net impact of the differential recruitment of GABAergic IN subtypes by recording layer 2/3 Pyr neurons with optogenetic suppression of specific types of GABAergic INs while activating different long-range inputs. Our results demonstrate that the preferential recruitment of VIP INs by wM1 disinhibits Pyr neurons in S1. We predict that the disinhibition in S1 driven by wM1 inputs may improve the detection of sensory stimuli during active sensation. In contrast, the strong recruitment of PV INs by S2 inputs results in strong feedforward inhibition within the supragranular layers of S1. Our result suggests that one possible role of S2 inputs could potentially be to enhance discriminability of sensory stimuli by sharpening sensory-evoked responses in S1. However, because of the strong reciprocal connections between S2 and S1, it has been difficult to identify which aspects of sensory processing are transmitted from S2 to S1 (Helmchen et al., 2018; Minamisawa et al., 2018; Ni and Chen, 2017; Petersen, 2019; Yamashita et al., 2018). Studies using calcium imaging and electrophysiological recordings support that S2 inputs to S1 carry information about task-relevant activity during whisker-dependent sensory perception tasks (Kwon et al., 2016; Sachidhanandam et al., 2013). S2 axons and layer 2/3 Pyr neurons in S1 showed enhanced activity, while PV INs exhibited diminished activity on correct trials. The enhanced activity of S1 Pyr neurons was most pronounced in the later component of stimulus-related responses. The circuit motif of S2-driven, PV IN-mediated feedforward inhibition in S1 in our present study seemingly contradicts these previous findings. We showed that S2 inputs dampen the response of layer 2/3 Pyr neurons in S1 by strongly recruiting PV INs. This may be due to learning-related synaptic plasticity in the projections from S2 to S1 during whisker-dependent sensory perception tasks. Supporting this idea, the increased activity in layer 2/3 Pyr neurons together with the reduced activity of PV INs in S1 was observed only after animals learned the sensory perception task but not from naive animals (Sachidhanandam et al., 2013). One possible explanation is that S2-driven, PV IN-mediated feedforward inhibition is a default circuit motif and task learning-related changes in the interaction between S1 and S2 may attenuate the recruitment of S1 PV INs by S2 inputs. In agreement with our finding, an anatomical study using a monosynaptic viral tracing method reported abundant S2 inputs to PV INs in S1 (Hafner et al., 2019).

In vivo optogenetic stimulation of POm combined with whisker stimulation evokes strong and long-lasting excitation in layer 2/3 Pyr neurons compared with wM1 and S2 stimulation (Zhang and Bruno, 2019). *Ex vivo* connectivity data including our study, however, demonstrated that direct synaptic input from POm to layer 2/3 Pyr neurons in S1 is not particularly prominent compared with other long-range inputs, including wM1 and S2 inputs, and is comparable with S1 GABAergic INs (Audette et al., 2018; Sermet et al., 2019). The strong engagement of layer 2/3 Pyr cells by POm input may be likely mediated by multisynaptic interactions. One possible mechanism is that thalamocortical and corticothalamic (CT) loops between POm and S1 lead to the stronger and long-lasting excitation of layer 2/3 Pyr neurons in S1. Nonetheless, reciprocal interactions also exist

between S1 and M1, and S1 and S2. Future studies will need to identify which features in the projection from POm to S1 support prominent excitation of layer 2/3 Pyr neurons in S1.

SST INs in long-range connection

Irrespective of input areas, our data show that SST INs in the supragranular layers of S1 are weakly connected by long-range excitatory inputs. Anatomically, monosynaptic tracing studies demonstrated that the amount of long-range presynaptic inputs to SST INs is comparable with other types of GABAergic cells (Wall et al., 2016). This indicates that the weak excitatory inputs to SST INs are likely due to weak synaptic strength. Considering the frequency-dependent facilitation of excitatory inputs to SST INs (Beierlein et al., 2003; Kapfer et al., 2007; Pouille and Scanziani, 2004; Reyes et al., 1998; Silberberg and Markram, 2007; Sylwestrak and Ghosh, 2012; Xu et al., 2013), it is possible that long-range excitatory inputs to SST INs were underestimated in our recordings because of low initial release probability. To test this possibility, we recorded from SST INs with a wide range of stimulation frequencies using ChETA, a fast variant of ChR2 (Gunaydin et al., 2010). Although SST INs did not show synaptic depression compared with nearby Pyr neurons, long-range excitatory synaptic inputs onto SST INs were not significantly facilitated. This result suggests that long-range excitatory inputs are not the main excitatory driver to SST INs. Instead, Pyr neurons in local networks serve as a main excitatory source to SST INs (Adesnik et al., 2012; Beierlein et al., 2003; Kapfer et al., 2007; Levy and Reyes, 2012; Pala and Petersen, 2015). Thus, SST INs function as a sensor of net local excitation and provide feedback inhibition in the local networks.

According to single-cell transcriptome studies, SST INs contain diverse subpopulations (Naka et al., 2019; Paul et al., 2017; Tasic et al., 2016; Zeisel et al., 2015). SST INs are diverse not only in their molecular and genetic profiles but also in their axonal morphology and intrinsic electrophysiological properties (Jiang et al., 2015; Ma et al., 2006; Muñoz et al., 2017; Naka et al., 2019; Nigro et al., 2018; Xu et al., 2013). More important, these studies provide evidence that the diverse subpopulation of SST INs differ in their local input and output connectivity, implying functionally distinct roles of different subtypes of SST INs during sensory processing (Jiang et al., 2015; Naka et al., 2019; Nigro et al., 2018; Xu et al., 2013). Our present study is restricted to neurons in the supragranular layers of S1. Morphologically, SST INs in the supragranular layers of S1 are mostly Martinotti cells, although the degree of their axonal innervation to layer 1 and layer 2/3 varies (Muñoz et al., 2017). Functionally, the majority of L2/3 SST INs show consistent modulation of their activity in relation to active sensory processing (Muñoz et al., 2017; Naka et al., 2019; Sachidhanandam et al., 2016; Yu et al., 2019). Thus, L2/3 SST INs appear to be a relatively homogeneous subpopulation of SST INs, while SST INs in infragranular layers are genetically, morphologically, and functionally diverse.

Similar to SST INs, the three other groups of cortical GABAergic INs also parse into multiple subtypes (He et al., 2016; Tasic et al., 2016, 2018). Emerging evidence indicates that different subtypes within each GABAergic IN type show distinct connectivity in a local circuit. Future studies will be required to address how the long-range connectivity rules apply to more refined GABAergic IN subtypes and to their laminar position. Although

activity flows throughout heavily interconnected cortical layers, each cortical layer has its own unique input, output, and local microcircuits. The present study was focused only on the supragranular layers of primary somatosensory cortex, which is a main gateway for cortico-cortical interactions. For example, POm inputs to different types of GABAergic INs in cortex has been reported to be layer-dependent (Audette et al., 2018; Sermet et al., 2019). Whether the same connectivity rules of long-range inputs are applied to GABAergic INs in other cortical layers needs to be tested.

Long-range inputs to Pyr neurons

We dwelled mostly on how different types of GABAergic neurons are preferentially recruited by diverse long-range inputs. Our present study considered excitatory Pyr neurons in the supragranular layers of S1 as one homogeneous population. Pyr neurons in the supragranular layers are mostly, if not all, of the intratelencephalic (IT) cell type projecting to other cortical areas and striatum, while those in infragranular layers consist of Pyr tract (PT), CT, and IT cell types (Gerfen et al., 2013; Greig et al., 2013; Harris and Shepherd, 2015; Huang, 2014; Shepherd, 2013). Although single-cell transcriptome studies indicate relatively less diversity among layer 2/3 Pyr neurons compared with those in other layers, these neurons can be further subdivided on the basis of their specific target areas within the cortex (Feldmeyer et al., 2013; Han et al., 2018; Sato and Svoboda, 2010; Yamashita et al., 2013). In the primary somatosensory cortex, for example, neurons that project to the primary motor cortex and the secondary somatosensory cortex mostly do not overlap, suggesting potential subpopulations of Pyr neurons within supragranular IT types, on the basis of their projection specificity (Feldmeyer et al., 2013; Sato and Svoboda, 2010; Yamashita et al., 2013). These neurons not only project to different brain areas in a non-overlapping manner, they also demonstrate distinct intrinsic properties and functional characteristics during sensorimotor processing. Our results indicate that although Pyr neurons in L2/3 of S1 received similar excitatory inputs from diverse input regions, the range of excitatory synaptic inputs to individual L2/3 Pyr neuron is widely distributed. There is a limitation in the direct comparison of optogenetic-evoked synaptic responses of Pyr cells from different inputs due to the variability of viral expression and the coverage of input areas. Yet the wide range of synaptic inputs may potentially reflect the subpopulations within the IT type of neurons. Future work is needed to address whether projection-based subpopulations of L2/3 Pyr neurons are differentially recruited by various long-range inputs.

STAR★METHODS

RESOURCE AVAILABILITY

Lead contact—Further information and requests for resources and reagents should be directed to and will be fulfilled by the Lead Contact, Soohyun Lee (soohyun.lee@nih.gov).

Materials availability—This study did not generate new unique reagents.

Data and code availability—The datasets and custom codes used for analyses have not been deposited in a public repository but are available from the corresponding author upon reasonable request.

EXPERIMENTAL MODEL AND SUBJECT DETAILS

All animal experiments were performed in accordance with an animal protocol approved by the National Institute of Mental Health (NIMH) Animal Care and Use Committee. Mice of either sex aged postnatal days 28 - 35 (for viral injections) or postnatal days 48 - 55 (for *ex vivo* brain slice recordings) were used for experiments. To target specific populations of GABAergic interneurons, we used the following transgenic mouse lines: Htr3a-BAC^{eGFP} for 5HT3aR INs, VIP-IRES-Cre for VIP INs, GIN and SST-IRES-Cre for SST INs, PV-Cre for PV INs, and Ai9 (RCL-tdT) tdTomato reporter mice. For anatomical experiments involving retro-Cre virus injection, Ai14 (RCL-tdT-D) tdTomato reporter mice were used. Mice heterozygous for the indicated genes were used for experiments. Mice were group-housed (up to 5 mice per cage) in a vivarium under reversed light-dark (12 h and 12 h) conditions with *ad libitum* access to food and water. Mice used in this study had no previous history of drug administration, surgery or behavioral testing. Both sexes of mice were used.

METHOD DETAILS

Stereotactic virus injection—Viral injection was performed on mice postnatal days 28-30. Mice were anesthetized in a chamber containing isoflurane (5%) and maintained under anesthesia in a stereotaxic apparatus (1%-1.5% isoflurane) (Leica Biosystems). Their body temperature was maintained at 35~37°C with a heating pad during the entire surgical procedure. A small incision was made in the scalp to expose the skull over the target area. The skull was thinned with a dental drill and a small craniotomy (~150 μm in diameter) was made. To target cS1, S2, wM1, POm, or ECt/PRh, following coordinates (in mm, measured from bregma) were used: wM1 (AP 1.0, ML 0.9), cS1 (AP −1.0, ML 3.4, 18° tilt), S2 (AP −1.5, ML 4.6, DV 2.3, 60° tilt), POm (AP −1.95, ML 1.30, DV −3.1), and ECt/Prh (AP −2.3, −2.6, ML 4.6, DV −3.5, 90° tilt). Adeno-associated viruses (AAVs) were used for the expression of channelrhodopsin (ChR2), halorhodopsin (NpHR). AAV5-CAG-hChR2(H134R)-mCherry-WPRE-SV40, AAV5-hSyn-hChR2(H134R)-eYFP, AAV1-hSyn-ChETA(E123T/H134R)-eYFP-WPRE-hGH, AAV5-EF1a-DIO-eNpHR3.0-EYFP and AAV5-EF1a-DIO-eNpHR3-mCherry were delivered using a glass micropipette (6-12 μm inner diameter) attached to a nanoliter injector (Nanoliter 2010, WPI). To target wM1, cS1, S2 or ECt/PRh, 15 nL of virus was injected every 100 μm from a depth of 800 μm to 200 μm over a 4 - 6 min period. To target POm, 60 nL was injected at a depth of 3.1 mm. To quantify neurons that project to superficial layers of S1 in a whole brain, rAAV2-retro-CAG-Cre was injected into layer 2/3 (50 nL at a depth of 250 μm) of S1 in Ai14 tdTomato reporter mouse line. After the injection, the pipette was held in the final position for 5-10 minutes before being retracted from the brain. During the surgery, both eyes of the animals were covered with a lubricating ointment. The incision was closed with absorbable sutures. All surgical procedures were performed under aseptic conditions. Mice were injected with meloxicam (5 mg/kg) daily for at least 3 days following surgery.

Tissue processing, automatic cell counting and immunohistochemistry—Three weeks after virus injection, mice were perfused transcardially with 4% paraformaldehyde (PFA) in PBS (pH 7.4). Brains were fixed in 4% PFA (in PBS) for 2 hours and were subsequently transferred to 30% sucrose (in PBS) overnight at 4°C. Coronal brain sections (50 μm thickness) were taken with a microtome (Leica Biosystems). Brain sections were

mounted and covered with an antifade mounting medium containing DAPI (Thermo Fisher Scientific). Tissues collected from the whole brain were imaged (Axio Scan, Zeiss). The scanned images were aligned to a standard coordinate system using the BrainMaker software (MBF Bioscience) and registered to the Allen Mouse Brain Common Coordinate Framework. Neurons labeled throughout the whole brain in the annotated reference atlas were automatically detected and subsequently quantified (NeuroInfo software, MBF Bioscience[96]).

For immunohistochemistry, brain sections (50 μm thickness) were collected in 0.1 M PBS. Sections were washed in PBS (2 times for 15 min) and incubated in a blocking solution (10% normal donkey serum, 1% BSA and 0.2% Triton X-100 in PBS) for 1 hour at room temperature (RT) under constant shaking. Brain sections were then incubated with primary antibodies (rabbit primary antibody for VIP, 1:200 dilution, 20077, ImmunoStar; mouse primary antibody for PV, 1:1,000 dilution, P3088, Millipore Sigma) in diluted blocking solution (1:10 dilution in PBS) overnight at 4°C. Brain sections were washed in PBS (3 times for 15 min) followed by 1 hour of secondary antibody incubation at RT. Alexa Fluor 647 conjugated secondary antibodies (A-31573, A-31571, 1:200 dilution, ThermoFisher Scientific) were used to visualize fluorescence signals. After 1 hour of incubation with secondary antibodies, sections were washed in PBS (3 times for 15 min), mounted on slides and coverslipped with antifade mounting medium containing DAPI (Thermo Fisher Scientific). Confocal images were acquired with a Zeiss LSM780 microscope.

Slice preparation for physiological experiments—Three weeks after virus injection, mice were anesthetized with isoflurane (5% isoflurane (vol/vol) in 100% oxygen), perfused transcardially with an ice-cold sucrose solution containing (in mM) 75 sucrose, 87 NaCl, 2.5 KCl, 26 $NaHCO_3$, 1.25 NaH_2PO_4, 10 glucose, 0.5 $CaCl_2$, and 2 $MgSO_4$, saturated with 95% O_2 and 5% CO_2 and decapitated. The brain was rapidly removed from the skull in a bath of ice-cold sucrose solution. Coronal slices of 300 μm were made using a vibratome (Leica Biosystems) and were stored in the same solution at 35° C for 30 min and at RT for an additional 30-45 min before recording.

***In vitro* electrophysiology and photostimulation—**Whole-cell patch clamp recordings were performed in oxygenated artificial cerebrospinal fluid (ACSF) containing (in mM) 125 NaCl, 2.5 KCl, 26 $NaHCO_3$, 1.25 NaH_2PO_4, 10 glucose, 2 $CaCl_2$ and 1 $MgCl_2$. The ACSF was equilibrated with 95% O2 and 5% CO2 throughout an entire recording session which typically lasted between 30 minutes to 1 hour. Recordings were performed at 30°C–33°C. Electrodes (3-7 MΩ) were pulled from borosilicate glass capillary (1.5 mm OD). The pipette intracellular solution contained (in mM) 130 potassium gluconate, 6.3 KCl, 0.5 EGTA, 10 HEPES, 5 sodium phosphocreatine, 4 Mg-ATP, 0.3 Na-GTP and 0.2% biocytin (pH 7.4 with KOH, 280-290 mOsm). Membrane potentials were not corrected for the liquid junction potential. During patching, cell-attached seal resistances were > 1 GΩ. Once whole-cell configuration was achieved, uncompensated series resistance was usually 5 – 30 MΩ and only cells with stable series resistance (< 20% change throughout the recording) were used for analysis. Data were collected using a Multiclamp 700B amplifier (Molecular Devices), low-pass filtered at 5 kHz and digitally sampled at 20 kHz, and

analyzed with pClamp10 (Molecular Devices). To characterize the intrinsic membrane properties of neurons, hyperpolarizing and depolarizing current steps were injected at 0.1 Hz under current-clamp configuration.

Photo-stimulation evoked EPSCs and EPSPs were recorded under voltage-clamp and current-clamp configuration, respectively. All intrinsic properties as well as light-evoked EPSPs were measured by holding cells at V_{rest}. Light-evoked EPSCs were measured while holding cells at −70 mV. For optogenetic stimulation, LED light was generated using a light emitting diode (LED) (470 nm and 590 nm) and controlled by a CoolLED pE-300^{ultra} system (CoolLED). Collimated light was delivered into the brain tissue through a 40X water-immersion objective. For the input mapping experiments, a train of photostimuli (10 pulses with 10 Hz and 3ms duration of each pulse) was delivered at 20 s intervals with the illumination intensity of 4 mW. In a subset of recordings, tetrodotoxin (TTX, 1 μM, Hello Bio Inc.) and 4-aminopyridine (4-AP) (100 μM, Hello Bio Inc.) was bath perfused to isolate direct monosynaptic inputs during optogenetic stimulation. To induce spontaneous activity in a subset of recordings, slices were perfused with a 'modified ACSF' containing (in mM) 126 NaCl, 5 KCl, 20 glucose, 26 $NaHCO_3$, 1.25 NaH_2PO_4, 1 $CaCl_2$ and 0.5 $MgSO_4$ (Neske and Connors, 2016). Brain tissues were perfused in a modified ACSF condition from the beginning in a recording chamber and electrophysiological recording was performed under the same modified ACSF condition. Spontaneous spiking activity was observed usually within 1 min under the modified ACSF superfusion. After the spontaneous activity reached a steady state, spikes were counted during a 1-minute time window.

CUBIC clearing of recorded tissue and streptavidin staining—After recording, brain slices were fixed in 4% PFA in 0.1M PB and kept overnight at 4°C and then kept in 20% sucrose (in PB). Slices were first washed with 0.1M PB (3 times for 10 min) at RT. Slices were then immersed in CUBIC reagent 1 (Susaki et al., 2014) for 2 days at 4°C. After 2 days of incubation, slices were washed with 0.1M PB (4 times for 30 min) at RT to ensure complete removal of CUBIC reagent 1. Slices were then incubated in fluorophore-conjugated streptavidin (1:500 dilution) (ThermoFisher Scientific) in 0.1M PB (0.5% Triton X-100), overnight at 4°C. Slices were subsequently washed with 0.1M PB (4 times, 30 min) at RT and mounted with CUBIC reagent 1. Neuronal morphology was imaged with a Zeiss LSM780 confocal microscope.

Electrophysiology analysis—The resting membrane potential of neurons (V_{rest}, in mV) was measured after the rupture of the neuronal membrane with no holding current applied. Intrinsic properties of neurons were measured under current-clamp configuration by applying current steps (800 msec duration). Input resistance (R_{in}, megaohms) was determined by measuring the voltage change in response to a step current injection (− 20 pA, 100 msec). To control the variability in the level of ChR2 expression in different brain slices, a pyramidal neuron was simultaneously recorded adjacent to an interneuron (< 200 μm) in the same brain slice. Photostimulation-evoked EPSCs or EPSPs were averaged across 20 sweeps and the peak amplitude was detected. Peak amplitude of the first response in a 10 Hz stimulus train recorded from an interneuron was normalized to the peak amplitude of the first response in a 10 Hz stimulus train from a nearby pyramidal neuron. Neurons were

excluded from analysis if photostimulation-evoked responses had a latency of > 4 msec (Figure S1). In order to assess synaptic dynamics, periodic light stimulations (10 pulses of 10 Hz, 3 msec pulse width) of 10, 20 and 50Hz were used. Amplitude of every EPSC in the stimulus train was normalized to the amplitude of the first EPSC.

Machine learning classifier analysis—We used a cross-validation procedure, with as many folds as the smallest number of data points in any combination of input region and GABAergic neuron type. For each fold, the data points in each combination were assigned into train (~75%) or test (~25%) groups. Within each of the groups, examples for each region were generated by taking every possible combination drawing one data point from each of the four neuron types. For instance, if the data points for region wM1 and the four neuron types were PV1/PV2, SST, nonVIP-5HTeGFP, VIP1/VIP2 (respectively 2, 1, 1, and 2 data points), we would have examples PV1 + SST + nonVIP-5HTeGFP + VIP1, PV2 + SST + nonVIP-5HTeGFP + VIP1, PV1 + SST + nonVIP-5HTeGFP + VIP2, and PV2 + SST + nonVIP-5HTeGFP + VIP2. Given that data points are entirely independent, the examples in each train and test set are also completely independent from each other. Furthermore, given that this process yielded different numbers of examples for each input region, we randomly sampled from regions with more examples so that the numbers were the same in the training set. The purpose of doing this was to prevent the classifier from biasing its prediction toward a more numerous class. We then used the training set to train a 5-way multinomial regression (using glmnet, selecting the optimal penalization parameter from a regularization path going from 10 to 0.00001, dividing by 10 at each step), and applied it to the test set to generate a region prediction for each example. We did this for all 4 folds, producing a label for all examples and an average accuracy value (percentage of examples for which the prediction was correct. In addition, this also allowed us to generate a confusion matrix, plotting the fraction of examples of region < i > that were classified as each of the 5 possible regions < j >. Given that this scheme generates examples stochastically, we averaged these results over 100 runs. In order to test the results, we had to take into account that the test examples are not independent from each other, since they share data points. This precludes the use of analytical tests for the results since these require independently drawn test examples. Instead, we used a permutation test procedure where we assumed that there were no region differences for each neuron type. This allows us to shuffle data points between regions for each GABAergic IN type while maintaining every other aspect of the experimental procedure. As expected, the 95% confidence interval for the average accuracy over 100 runs was 0.20 ± 0.012 (chance level), and performance with the original labels was always higher than in any of the shuffled runs. This indicates that the results are significant at a level of $p < 0.01$.

QUANTIFICATION AND STATISTICAL ANALYSIS

Data has been presented throughout as mean ± s.e.m (standard error of the mean) unless otherwise noted. Unless indicated, all statistical comparisons were non-parametric. Collection of data and analysis of the same were not performed blind and were non-randomized. No statistical methods were employed to pre-determine sample sizes. Number of recorded neurons (n) and number of animals (N) used were reported for each figure. All data were analyzed using pClamp10, GraphPad Prism and custom written MATLAB

software. Information on statistical tests used for analysis and p values can be found in the main text and in the figure legends.

Supplementary Material

Refer to Web version on PubMed Central for supplementary material.

ACKNOWLEDGMENTS

This work was supported by the Intramural Research Program of National Institute of Mental Health, National Institutes of Health (ZIAMH002959). We thank Drs. A. Lourenco Inacio, C.J. McBain, K.A. Pelkey, R. Chittajallu, and T.J. Petros for helpful comments on the manuscript. We thank all members of the Lee lab, the McBain lab, the Petros lab, and the Lu lab for helpful discussions. We thank the NIMH Systems Neuroscience Imaging Resource for assistance with histological analyses and the NIMH Rodent Behavioral Core for providing surgical setup.

REFERENCES

Abs E, Poorthuis RB, Apelblat D, Muhammad K, Pardi MB, Enke L, Kushinsky D, Pu DL, Eizinger MF, Conzelmann KK, et al. (2018). Learning-related plasticity in dendrite-targeting layer 1 interneurons. Neuron 100, 684–699.e6. [PubMed: 30269988]

Adesnik H, Bruns W, Taniguchi H, Huang ZJ, and Scanziani M (2012). A neural circuit for spatial summation in visual cortex. Nature 490, 226–231. [PubMed: 23060193]

Adler A, Zhao R, Shin ME, Yasuda R, and Gan WB (2019). Somatostatin-expressing interneurons enable and maintain learning-dependent sequential activation of pyramidal neurons. Neuron 102, 202–216.e7. [PubMed: 30792151]

Alitto HJ, and Dan Y (2013). Cell-type-specific modulation of neocortical activity by basal forebrain input. Front. Syst. Neurosci 6, 79. [PubMed: 23316142]

Aronoff R, Matyas F, Mateo C, Ciron C, Schneider B, and Petersen CC (2010). Long-range connectivity of mouse primary somatosensory barrel cortex. Eur. J. Neurosci 31, 2221–2233. [PubMed: 20550566]

Audette NJ, Urban-Ciecko J, Matsushita M, and Barth AL (2018). POm thalamocortical input drives layer-specific microcircuits in somatosensory cortex. Cereb. Cortex 28, 1312–1328. [PubMed: 28334225]

Bakken TE, Hodge RD, Miller JA, Yao Z, Nguyen TN, Aevermann B, Barkan E, Bertagnolli D, Casper T, Dee N, et al. (2018). Single-nucleus and single-cell transcriptomes compared in matched cortical cell types. PLoS ONE 13, e0209648. [PubMed: 30586455]

Batista-Brito R, Vinck M, Ferguson KA, Chang JT, Laubender D, Lur G, Mossner JM, Hernandez VG, Ramakrishnan C, Deisseroth K, et al. (2017). Developmental dysfunction of VIP interneurons impairs cortical circuits. Neuron 95, 884–895.e9. [PubMed: 28817803]

Batista-Brito R, Zagha E, Ratliff JM, and Vinck M (2018). Modulation of cortical circuits by top-down processing and arousal state in health and disease. Curr. Opin. Neurobiol 52, 172–181. [PubMed: 30064117]

Beierlein M, Gibson JR, and Connors BW (2003). Two dynamically distinct inhibitory networks in layer 4 of the neocortex. J. Neurophysiol 90, 2987–3000. [PubMed: 12815025]

Chamberland S, and Topolnik L (2012). Inhibitory control of hippocampal inhibitory neurons. Front. Neurosci 6, 165. [PubMed: 23162426]

Chen JL, Carta S, Soldado-Magraner J, Schneider BL, and Helmchen F (2013). Behaviour-dependent recruitment of long-range projection neurons in somatosensory cortex. Nature 499, 336–340. [PubMed: 23792559]

Cichon J, Blanck TJJ, Gan WB, and Yang G (2017). Activation of cortical somatostatin interneurons prevents the development of neuropathic pain. Nat. Neurosci 20, 1122–1132. [PubMed: 28671692]

DeNardo LA, Berns DS, DeLoach K, and Luo L (2015). Connectivity of mouse somatosensory and prefrontal cortex examined with trans-synaptic tracing. Nat. Neurosci 18, 1687–1697. [PubMed: 26457553]

Dipoppa M, Ranson A, Krumin M, Pachitariu M, Carandini M, and Harris KD (2018). Vision and locomotion shape the interactions between neuron types in mouse visual cortex. Neuron 98, 602–615.e8. [PubMed: 29656873]

Eastwood BS, Hooks BM, Paletzki RF, O'Connor NJ, Glaser JR, and Gerfen CR (2019). Whole mouse brain reconstruction and registration to a reference atlas with standard histochemical processing of coronal sections. J. Comp. Neurol 527, 2170–2178. [PubMed: 30549030]

Feldmeyer D, Brecht M, Helmchen F, Petersen CC, Poulet JF, Staiger JF, Luhmann HJ, and Schwarz C (2013). Barrel cortex function. Prog. Neurobiol 103, 3–27. [PubMed: 23195880]

Fishell G, and Kepecs A (2019). Interneuron types as attractors and controllers. Annu. Rev. Neurosci 43, 1–30. [PubMed: 31299170]

Fu Y, Tucciarone JM, Espinosa JS, Sheng N, Darcy DP, Nicoll RA, Huang ZJ, and Stryker MP (2014). A cortical circuit for gain control by behavioral state. Cell 156, 1139–1152. [PubMed: 24630718]

Gentet LJ, Kremer Y, Taniguchi H, Huang ZJ, Staiger JF, and Petersen CC (2012). Unique functional properties of somatostatin-expressing GABAergic neurons in mouse barrel cortex. Nat. Neurosci 15, 607–612. [PubMed: 22366760]

Gerfen CR, Paletzki R, and Heintz N (2013). GENSAT BAC cre-recombinase driver lines to study the functional organization of cerebral cortical and basal ganglia circuits. Neuron 80, 1368–1383. [PubMed: 24360541]

Gilbert CD, and Li W (2013). Top-down influences on visual processing. Nat. Rev. Neurosci 14, 350–363. [PubMed: 23595013]

Greig LC, Woodworth MB, Galazo MJ, Padmanabhan H, and Macklis JD (2013). Molecular logic of neocortical projection neuron specification, development and diversity. Nat. Rev. Neurosci 14, 755–769. [PubMed: 24105342]

Gunaydin LA, Yizhar O, Berndt A, Sohal VS, Deisseroth K, and Hegemann P (2010). Ultrafast optogenetic control. Nat. Neurosci 13, 387–392. [PubMed: 20081849]

Hafner G, Witte M, Guy J, Subhashini N, Fenno LE, Ramakrishnan C, Kim YS, Deisseroth K, Callaway EM, Oberhuber M, et al. (2019). Mapping brain-wide afferent inputs of parvalbumin-expressing GABAergic neurons in barrel cortex reveals local and long-range circuit motifs. Cell Rep. 28, 3450–3461.e8. [PubMed: 31553913]

Han Y, Kebschull JM, Campbell RAA, Cowan D, Imhof F, Zador AM, and Mrsic-Flogel TD (2018). The logic of single-cell projections from visual cortex. Nature 556, 51–56. [PubMed: 29590093]

Hangya B, Pi HJ, Kvitsiani D, Ranade SP, and Kepecs A (2014). From circuit motifs to computations: mapping the behavioral repertoire of cortical interneurons. Curr. Opin. Neurobiol 26, 117–124. [PubMed: 24508565]

Harris KD, and Shepherd GM (2015). The neocortical circuit: themes and variations. Nat. Neurosci 18, 170–181. [PubMed: 25622573]

He M, Tucciarone J, Lee S, Nigro MJ, Kim Y, Levine JM, Kelly SM, Krugikov I, Wu P, Chen Y, et al. (2016). Strategies and tools for combinatorial targeting of GABAergic neurons in mouse cerebral cortex. Neuron 92, 555.

Helmchen F, Gilad A, and Chen JL (2018). Neocortical dynamics during whisker-based sensory discrimination in head-restrained mice. Neuroscience 368, 57–69. [PubMed: 28919043]

Hooks BM (2017). Sensorimotor convergence in circuitry of the motor cortex. Neuroscientist 23, 251–263. [PubMed: 27091827]

Huang ZJ (2014). Toward a genetic dissection of cortical circuits in the mouse. Neuron 83, 1284–1302. [PubMed: 25233312]

Jiang X, Shen S, Cadwell CR, Berens P, Sinz F, Ecker AS, Patel S, and Tolias AS (2015). Principles of connectivity among morphologically defined cell types in adult neocortex. Science 350, aac9462. [PubMed: 26612957]

Kapfer C, Glickfeld LL, Atallah BV, and Scanziani M (2007). Supralinear increase of recurrent inhibition during sparse activity in the somatosensory cortex. Nat. Neurosci 10, 743–753. [PubMed: 17515899]

Karnani MM, Jackson J, Ayzenshtat I, Tucciarone J, Manoocheri K, Snider WG, and Yuste R (2016). Cooperative subnetworks of molecularly similar interneurons in mouse neocortex. Neuron 90, 86–100. [PubMed: 27021171]

Kawaguchi Y, and Kubota Y (1997). GABAergic cell subtypes and their synaptic connections in rat frontal cortex. Cereb. Cortex 7, 476–486. [PubMed: 9276173]

Khan AG, and Hofer SB (2018). Contextual signals in visual cortex. Curr. Opin. Neurobiol 52, 131–138. [PubMed: 29883940]

Kubota Y (2014). Untangling GABAergic wiring in the cortical microcircuit. Curr. Opin. Neurobiol 26, 7–14. [PubMed: 24650498]

Kuchibhotla KV, Gill JV, Lindsay GW, Papadoyannis ES, Field RE, Sten TA, Miller KD, and Froemke RC (2017). Parallel processing by cortical inhibition enables context-dependent behavior. Nat. Neurosci 20, 62–71. [PubMed: 27798631]

Kvitsiani D, Ranade S, Hangya B, Taniguchi H, Huang JZ, and Kepecs A (2013). Distinct behavioural and network correlates of two interneuron types in prefrontal cortex. Nature 498, 363–366. [PubMed: 23708967]

Kwon SE, Yang H, Minamisawa G, and O'Connor DH (2016). Sensory and decision-related activity propagate in a cortical feedback loop during touch perception. Nat. Neurosci 19, 1243–1249. [PubMed: 27437910]

Larkum M (2013). A cellular mechanism for cortical associations: an organizing principle for the cerebral cortex. Trends Neurosci. 36, 141–151. [PubMed: 23273272]

Lee S, Hjerling-Leffler J, Zagha E, Fishell G, and Rudy B (2010). The largest group of superficial neocortical GABAergic interneurons expresses ionotropic serotonin receptors. J. Neurosci 30, 16796–16808. [PubMed: 21159951]

Lee S, Kruglikov I, Huang ZJ, Fishell G, and Rudy B (2013). A disinhibitory circuit mediates motor integration in the somatosensory cortex. Nat. Neurosci 16, 1662–1670. [PubMed: 24097044]

Lee AT, Cunniff MM, See JZ, Wilke SA, Luongo FJ, Ellwood IT, Ponnavolu S, and Sohal VS (2019). VIP interneurons contribute to avoidance behavior by regulating information flow across hippocampal-prefrontal networks. Neuron 102, 1223–1234.e4. [PubMed: 31053407]

Letzkus JJ, Wolff SB, Meyer EM, Tovote P, Courtin J, Herry C, and Lüthi A (2011). A disinhibitory microcircuit for associative fear learning in the auditory cortex. Nature 480, 331–335. [PubMed: 22158104]

Levy RB, and Reyes AD (2012). Spatial profile of excitatory and inhibitory synaptic connectivity in mouse primary auditory cortex. J. Neurosci 32, 5609–5619. [PubMed: 22514322]

Ma Y, Hu H, Berrebi AS, Mathers PH, and Agmon A (2006). Distinct subtypes of somatostatin-containing neocortical interneurons revealed in transgenic mice. J. Neurosci 26, 5069–5082. [PubMed: 16687498]

Madisen L, Zwingman TA, Sunkin SM, Oh SW, Zariwala HA, Gu H, Ng LL, Palmiter RD, Hawrylycz MJ, Jones AR, et al. (2010). A robust and high-throughput Cre reporting and characterization system for the whole mouse brain. Nat. Neurosci 13, 133–140. [PubMed: 20023653]

Manita S, Suzuki T, Homma C, Matsumoto T, Odagawa M, Yamada K, Ota K, Matsubara C, Inutsuka A, Sato M, et al. (2015). A top-down cortical circuit for accurate sensory perception. Neuron 86, 1304–1316. [PubMed: 26004915]

Marques T, Nguyen J, Fioreze G, and Petreanu L (2018). The functional organization of cortical feedback inputs to primary visual cortex. Nat. Neurosci 21, 757–764. [PubMed: 29662217]

Meyer K (2011). Primary sensory cortices, top-down projections and conscious experience. Prog. Neurobiol 94, 408–417. [PubMed: 21683755]

Minamisawa G, Kwon SE, Chevée M, Brown SP, and O'Connor DH (2018). A non-canonical feedback circuit for rapid interactions between somatosensory cortices. Cell Rep. 23, 2718–2731.e6. [PubMed: 29847801]

Muñoz W, Tremblay R, Levenstein D, and Rudy B (2017). Layer-specific modulation of neocortical dendritic inhibition during active wakefulness. Science 355, 954–959. [PubMed: 28254942]

Naka A, Veit J, Shababo B, Chance RK, Risso D, Stafford D, Snyder B,Egladyous A, Chu D, Sridharan S, et al. (2019). Complementary networks of cortical somatostatin interneurons enforce layer specific control. eLife 8, e43696. [PubMed: 30883329]

Neske GT, and Connors BW (2016). Distinct roles of SOM and VIP interneurons during cortical up states. Front. Neural Circuits 10, 52. [PubMed: 27507936]

Ni J, and Chen JL (2017). Long-range cortical dynamics: a perspective from the mouse sensorimotor whisker system. Eur. J. Neurosci 46, 2315–2324. [PubMed: 28921729]

Nigro MJ, Hashikawa-Yamasaki Y, and Rudy B (2018). Diversity and connectivity of layer 5 somatostatin-expressing interneurons in the mouse barrel cortex. J. Neurosci 38, 1622–1633. [PubMed: 29326172]

Oh SW, Harris JA, Ng L, Winslow B, Cain N, Mihalas S, Wang Q, Lau C, Kuan L, Henry AM, et al. (2014). A mesoscale connectome of the mouse brain. Nature 508, 207–214. [PubMed: 24695228]

Pala A, and Petersen CCH (2015). In vivo measurement of cell-type-specific synaptic connectivity and synaptic transmission in layer 2/3 mouse barrel cortex. Neuron 85, 68–75. [PubMed: 25543458]

Palmer LM, Schulz JM, Murphy SC, Ledergerber D, Murayama M, and Larkum ME (2012). The cellular basis of GABA(B)-mediated interhemispheric inhibition. Science 335, 989–993. [PubMed: 22363012]

Paul A, Crow M, Raudales R, He M, Gillis J, and Huang ZJ (2017). Transcriptional architecture of synaptic communication delineates GABAergic neuron identity. Cell 171, 522–539.e20. [PubMed: 28942923]

Pelkey KA, Chittajallu R, Craig MT, Tricoire L, Wester JC, and McBain CJ (2017). Hippocampal GABAergic inhibitory interneurons. Physiol. Rev 97, 1619–1747. [PubMed: 28954853]

Petersen CCH (2019). Sensorimotor processing in the rodent barrel cortex. Nat. Rev. Neurosci 20, 533–546. [PubMed: 31367018]

Petreanu L, Mao T, Sternson SM, and Svoboda K (2009). The subcellular organization of neocortical excitatory connections. Nature 457, 1142–1145. [PubMed: 19151697]

Pfeffer CK, Xue M, He M, Huang ZJ, and Scanziani M (2013). Inhibition of inhibition in visual cortex: the logic of connections between molecularly distinct interneurons. Nat. Neurosci 16, 1068–1076. [PubMed: 23817549]

Pi HJ, Hangya B, Kvitsiani D, Sanders JI, Huang ZJ, and Kepecs A (2013). Cortical interneurons that specialize in disinhibitory control. Nature 503, 521–524. [PubMed: 24097352]

Pouille F, and Scanziani M (2004). Routing of spike series by dynamic circuits in the hippocampus. Nature 429, 717–723. [PubMed: 15170216]

Reyes A, Lujan R, Rozov A, Burnashev N, Somogyi P, and Sakmann B (1998). Target-cell-specific facilitation and depression in neocortical circuits. Nat. Neurosci 1, 279–285. [PubMed: 10195160]

Sachidhanandam S, Sreenivasan V, Kyriakatos A, Kremer Y, and Petersen CC (2013). Membrane potential correlates of sensory perception in mouse barrel cortex. Nat. Neurosci 16, 1671–1677. [PubMed: 24097038]

Sachidhanandam S, Sermet BS, and Petersen CCH (2016). Parvalbumin-expressing GABAergic neurons in mouse barrel cortex contribute to gating a goal-directed sensorimotor transformation. Cell Rep. 15, 700–706. [PubMed: 27149853]

Sato TR, and Svoboda K (2010). The functional properties of barrel cortex neurons projecting to the primary motor cortex. J. Neurosci 30, 4256–4260. [PubMed: 20335461]

Schneider DM, Nelson A, and Mooney R (2014). A synaptic and circuit basis for corollary discharge in the auditory cortex. Nature 513, 189–194. [PubMed: 25162524]

Sermet BS, Truschow P, Feyerabend M, Mayrhofer JM, Oram TB, Yizhar O, Staiger JF, and Petersen CC (2019). Pathway-, layer- and cell-type-specific thalamic input to mouse barrel cortex. eLife 8, e52665. [PubMed: 31860443]

Shepherd GM (2013). Corticostriatal connectivity and its role in disease. Nat. Rev. Neurosci 14, 278–291. [PubMed: 23511908]

Silberberg G, and Markram H (2007). Disynaptic inhibition between neocortical pyramidal cells mediated by Martinotti cells. Neuron 53, 735–746. [PubMed: 17329212]

Susaki EA, Tainaka K, Perrin D, Kishino F, Tawara T, Watanabe TM, Yokoyama C, Onoe H, Eguchi M, Yamaguchi S, et al. (2014). Whole-brain imaging with single-cell resolution using chemical cocktails and computational analysis. Cell 157, 726–739. [PubMed: 24746791]

Sylwestrak EL, and Ghosh A (2012). Elfn1 regulates target-specific release probability at CA1-interneuron synapses. Science 338, 536–540. [PubMed: 23042292]

Tasic B, Menon V, Nguyen TN, Kim TK, Jarsky T, Yao Z, Levi B, Gray LT, Sorensen SA, Dolbeare T, et al. (2016). Adult mouse cortical cell taxonomy revealed by single cell transcriptomics. Nat. Neurosci 19, 335–346. [PubMed: 26727548]

Tasic B, Yao Z, Graybuck LT, Smith KA, Nguyen TN, Bertagnolli D, Goldy J, Garren E, Economo MN, Viswanathan S, et al. (2018). Shared and distinct transcriptomic cell types across neocortical areas. Nature 563, 72–78. [PubMed: 30382198]

Tervo DG, Hwang BY, Viswanathan S, Gaj T, Lavzin M, Ritola KD, Lindo S, Michael S, Kuleshova E, Ojala D, et al. (2016). A designer AAV variant permits efficient retrograde access to projection neurons. Neuron 92, 372–382. [PubMed: 27720486]

Tremblay R, Lee S, and Rudy B (2016). GABAergic interneurons in the neocortex: from cellular properties to circuits. Neuron 91, 260–292. [PubMed: 27477017]

Turi GF, Li WK, Chavlis S, Pandi I, O'Hare J, Priestley JB, Grosmark AD, Liao Z, Ladow M, Zhang JF, et al. (2019). Vasoactive intestinal polypeptide-expressing interneurons in the hippocampus support goal-oriented spatial learning. Neuron 101, 1150–1165.e8. [PubMed: 30713030]

Van Essen DC, Anderson CH, and Felleman DJ (1992). Information processing in the primate visual system: an integrated systems perspective. Science 255, 419–423. [PubMed: 1734518]

Wall NR, De La Parra M, Sorokin JM, Taniguchi H, Huang ZJ, and Callaway EM (2016). Brain-wide maps of synaptic input to cortical interneurons. J. Neurosci 36, 4000–4009. [PubMed: 27053207]

Wang Y, Toledo-Rodriguez M, Gupta A, Wu C, Silberberg G, Luo J, and Markram H (2004). Anatomical, physiological and molecular properties of Martinotti cells in the somatosensory cortex of the juvenile rat. J. Physiol 561, 65–90. [PubMed: 15331670]

Wimmer VC, Bruno RM, de Kock CP, Kuner T, and Sakmann B (2010). Dimensions of a projection column and architecture of VPM and POm axons in rat vibrissal cortex. Cereb. Cortex 20, 2265–2276. [PubMed: 20453248]

Xu H, Jeong HY, Tremblay R, and Rudy B (2013). Neocortical somatostatin-expressing GABAergic interneurons disinhibit the thalamorecipient layer 4. Neuron 77, 155–167. [PubMed: 23312523]

Xu H, Liu L, Tian Y, Wang J, Li J, Zheng J, Zhao H, He M, Xu TL, Duan S, and Xu H (2019). A disinhibitory microcircuit mediates conditioned social fear in the prefrontal cortex. Neuron 102, 668–682.e5. [PubMed: 30898376]

Yamashita T, Pala A, Pedrido L, Kremer Y, Welker E, and Petersen CC (2013). Membrane potential dynamics of neocortical projection neurons driving target-specific signals. Neuron 80, 1477–1490. [PubMed: 24360548]

Yamashita T, Vavladeli A, Pala A, Galan K, Crochet S, Petersen SSA, and Petersen CCH (2018). Diverse long-range axonal projections of excitatory layer 2/3 neurons in mouse barrel cortex. Front. Neuroanat 12, 33. [PubMed: 29765308]

Yu J, Hu H, Agmon A, and Svoboda K (2019). Recruitment of GABAergic interneurons in the barrel cortex during active tactile behavior. Neuron 104, 412–427.e4. [PubMed: 31466734]

Zeisel A, Muñoz-Manchado AB, Codeluppi S, Lönnerberg P, La Manno G, Juréus A, Marques S, Munguba H, He L, Betsholtz C, et al. (2015). Brain structure. Cell types in the mouse cortex and hippocampus revealed by single-cell RNA-seq. Science 347, 1138–1142. [PubMed: 25700174]

Zhang W, and Bruno RM (2019). High-order thalamic inputs to primary somatosensory cortex are stronger and longer lasting than cortical inputs. eLife 8, e44158. [PubMed: 30741160]

Zhang S, Xu M, Kamigaki T, Hoang Do JP, Chang WC, Jenvay S, Miyamichi K, Luo L, and Dan Y (2014). Selective attention. Long-range and local circuits for top-down modulation of visual cortex processing. Science 345, 660–665. [PubMed: 25104383]

Zingg B, Hintiryan H, Gou L, Song MY, Bay M, Bienkowski MS, Foster NN, Yamashita S, Bowman I, Toga AW, and Dong HW (2014). Neural networks of the mouse neocortex. Cell 156, 1096–1111. [PubMed: 24581503]

Highlights

- Diverse long-range inputs engage distinct GABAergic neurons in S1
- S2 inputs recruit PV neurons leading to feedforward inhibition of pyramidal cells in S1
- M1 inputs recruit VIP neurons leading to disinhibition of pyramidal cells in S1
- SST neurons receive relatively weak long-range inputs regardless of input area

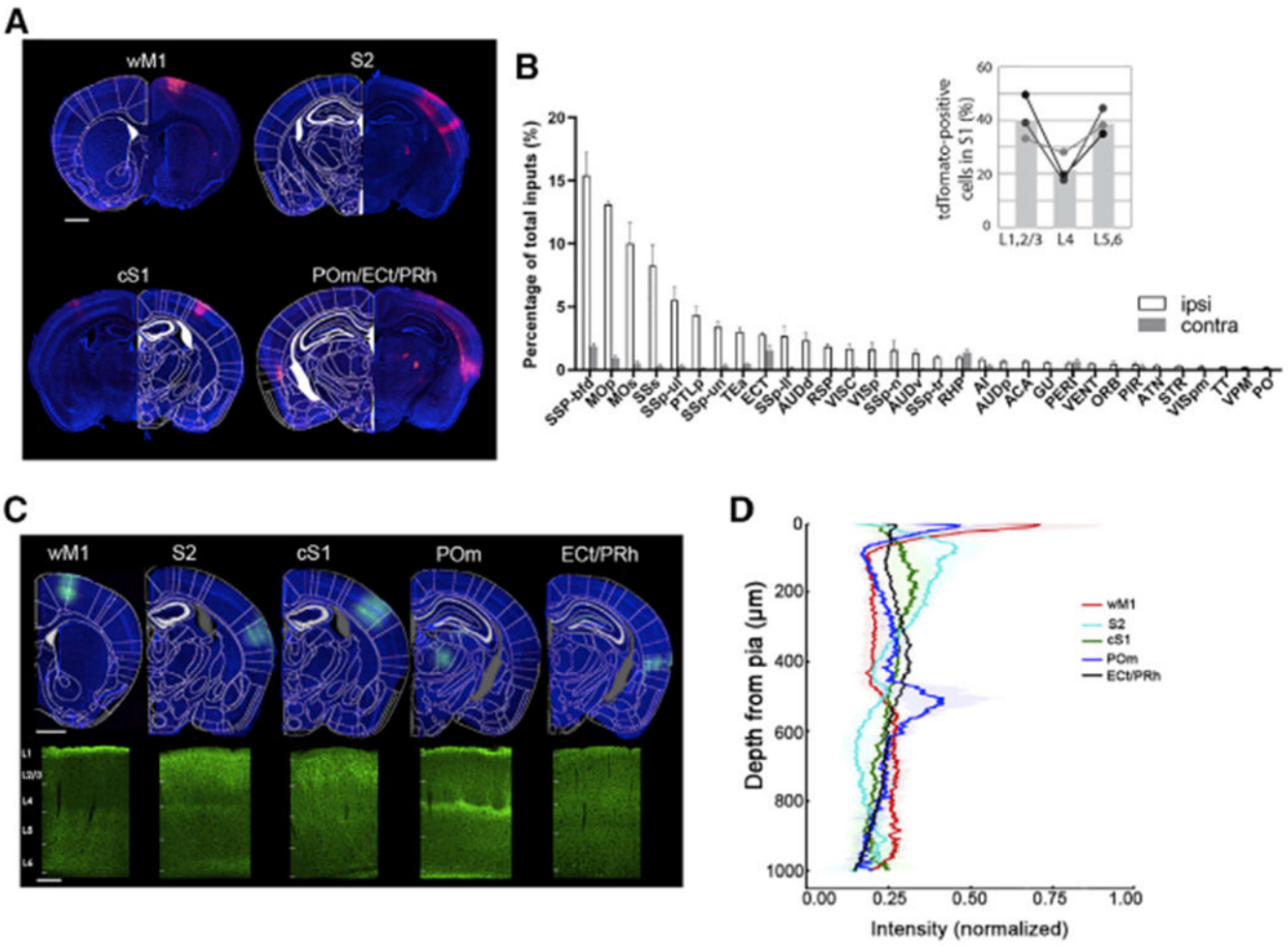

Figure 1. Whole-brain mapping of diverse long-range input areas to the supragranular layers of S1

(A) rAAV2retro-cre virus was unilaterally injected into supragranular layers of S1 in Ai14 mice. Representative coronal sections show the labeled input neurons in different brain areas. Scale bar, 1 mm.

(B) Whole-brain quantification of retrogradely labeled neurons. Open and gray bars show the inputs from ipsilateral and contralateral brain areas, respectively. Abbreviations for the different brain areas are given according to the Allen Brain Atlas (N = 3 mice). The inset shows the laminar distribution of tdTomato-positive cells within S1.

(C) Top panel: expression of ChR2-eYFP in diverse long-range input areas including wM1, S2, cS1, ECt/PRh, and POm. Scale bar, 1 mm. Bottom panel: labeling of long-range projection axons in S1 with eYFP, scale bar, 200 µm. Cortical layers are demarcated.

(D) Laminar distribution of eYFP-expressing axons from diverse brain areas innervating S1. Proportion of pixel intensity of eYFP expression to the total intensity from pia to white matter was plotted against cortical depth. Six S1 images from two mice were analyzed per input area; shading indicates SD.

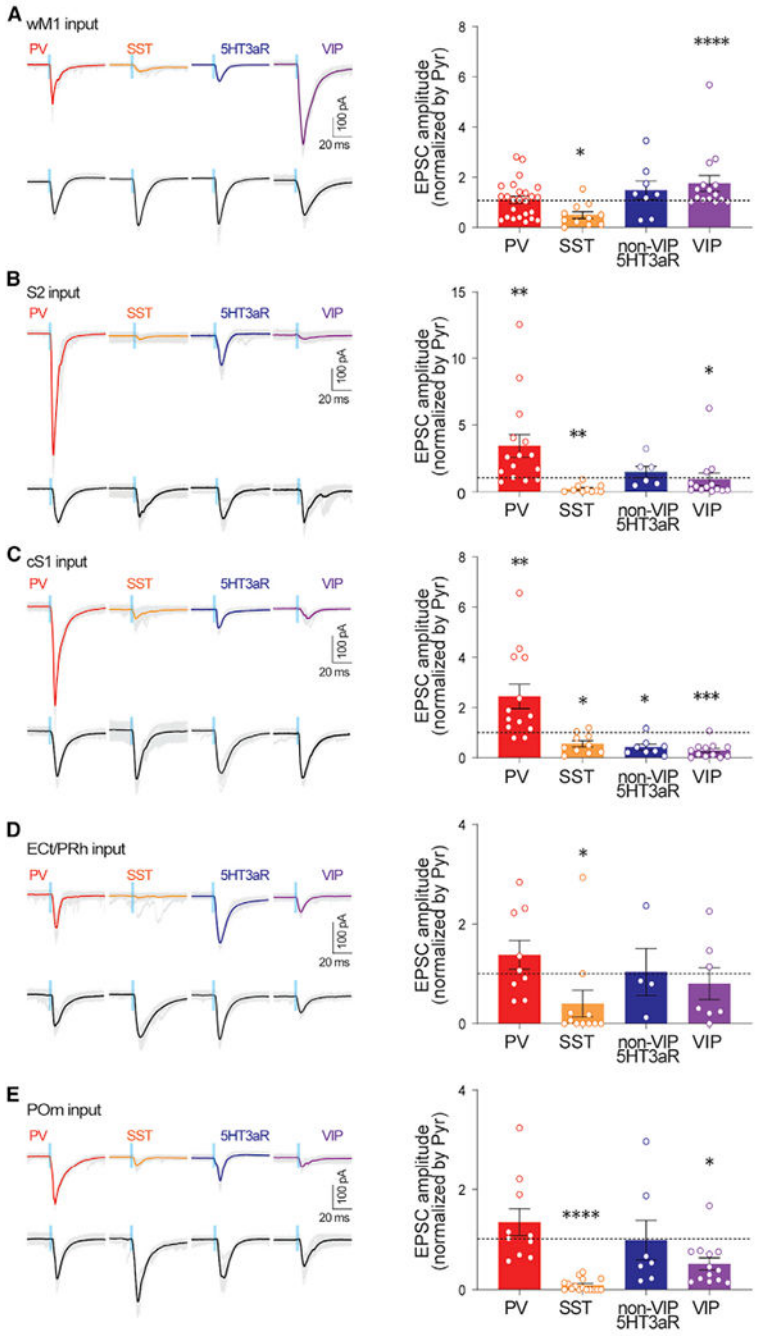

Figure 2. Long-range inputs from diverse brain areas differentially engage different subtypes of GABAergic neurons in the supragranular layers of S1

Left: example traces of ChR2 photostimulation-evoked EPSCs from PV INs, SST INs, nonVIP-5HT3aR INs, VIP INs, and Pyr from wM1, S2, cS1, ECt/PRh, and POm. Gray traces depict individual sweeps, and solid traces indicate the average of these sweeps. Blue bar indicates ChR2 photostimulation (470 nm, 3 ms). Right: population data showing EPSCs of GABAergic INs normalized to those of simultaneously recorded nearby pyramidal neurons. *$p < 0.05$, **$p < 0.005$, and ***$p < 0.0005$ (Wilcoxon signed-rank test). See also Figures S1–S4.

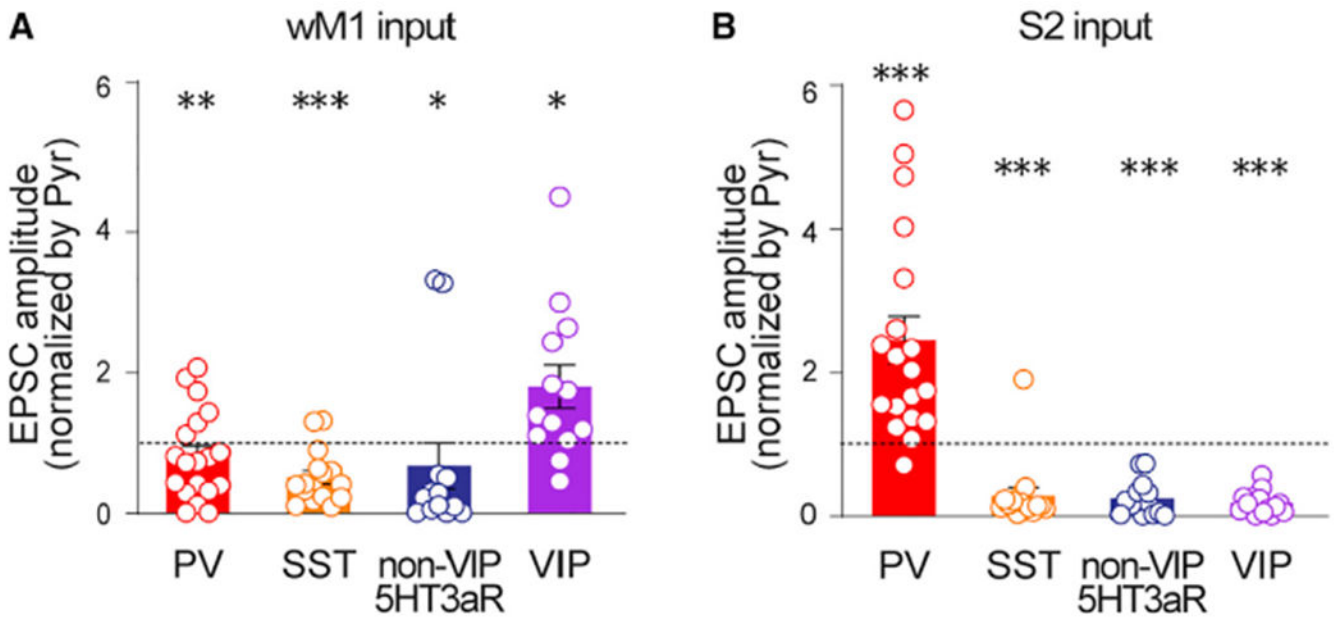

Figure 3. Monosynaptic long-range inputs from wM1 and S2 differentially engage different subtypes of GABAergic neurons in the supragranular layers of S1

Population data showing EPSCs of GABAergic INs normalized to those of simultaneously recorded nearby pyramidal neurons for wM1 (A) (GABAergic INs, mean ± SEM, number of recorded neurons, number of mice used, p value; PV INs, 0.78 ± 0.14, 19, 4, **p = 0.0071; SST INs, 0.48 ± 0.09, 16, 3, ***p = 0.0002; nonVIP-5HT3aR INs, 0.65 ± 0.31, 13, 3, *p = 0.0171; VIP INs, 1.75 ± 0.29, 13, 4, *p = 0.0215) and S2 (B) (GABAergic INs, mean ± SEM, number of recorded neurons, number of mice used, p value; PV INs, 2.44 ± 0.33, 19, 3, ****p < 0.0001; SST INs, 0.27 ± 0.11, 15, 3, ***p = 0.0002; nonVIP-5HT3aR INs, 0.23 ± 0.06, 14, 3, ***p = 0.0001; VIP INs, 0.17 ± 0.04, 14, 3, ***p = 0.0001) inputs, respectively. Recordings were performed in the presence of TTX and 4-AP. *p < 0.05, **p < 0.005, and ***p < 0.0005 (Wilcoxon signed-rank test). See also Figures S1–S3.

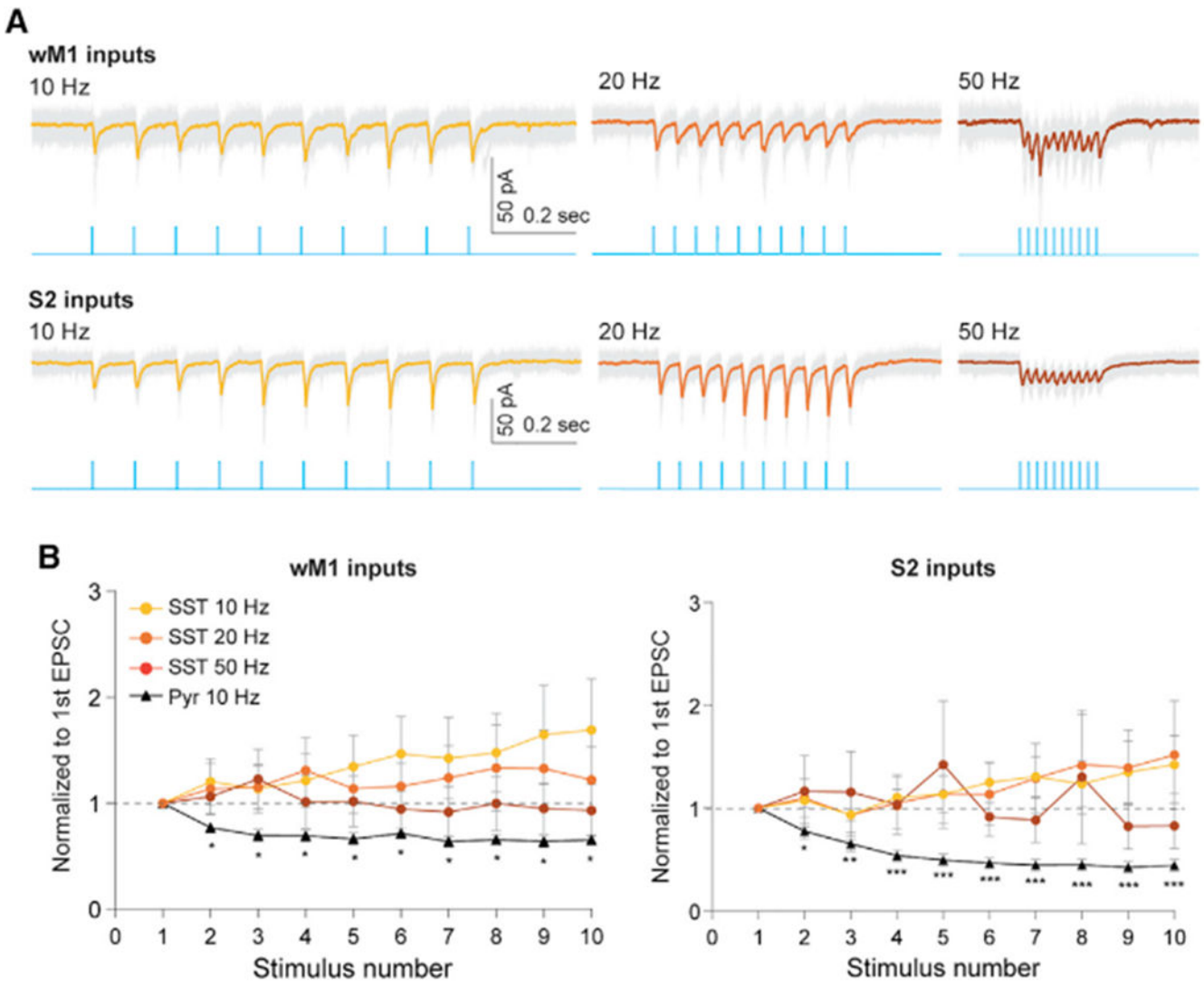

Figure 4. Synaptic dynamics of SST INs to long-range excitatory inputs

(A) Example traces showing EPSC responses of SST INs to a wide range of photostimulation frequencies of wM1 (top panel) and S2 (bottom panel) inputs. Blue traces indicate train of photostimulation (470 nm, ten pulses, 3 ms duration) delivered at 10, 20, and 50 Hz. Gray traces depict individual sweeps, colored traces indicate the average of these sweeps.

(B) Population data of SST INs (circle) and Pyr neurons (triangle) showing short-term dynamics upon stimulation of wM1 (left) and S2 (right) inputs. Although EPSC amplitudes in Pyr neurons were strongly attenuated, EPSCs recorded from SST INs were stable over a wide range of stimulation frequencies. The peak amplitude of the EPSCs in each cell was normalized to that of the first EPSC. *$p < 0.05$, **$p < 0.05$, and ***$p < 0.0005$ (Wilcoxon signed-rank test).

See also Figure S5.

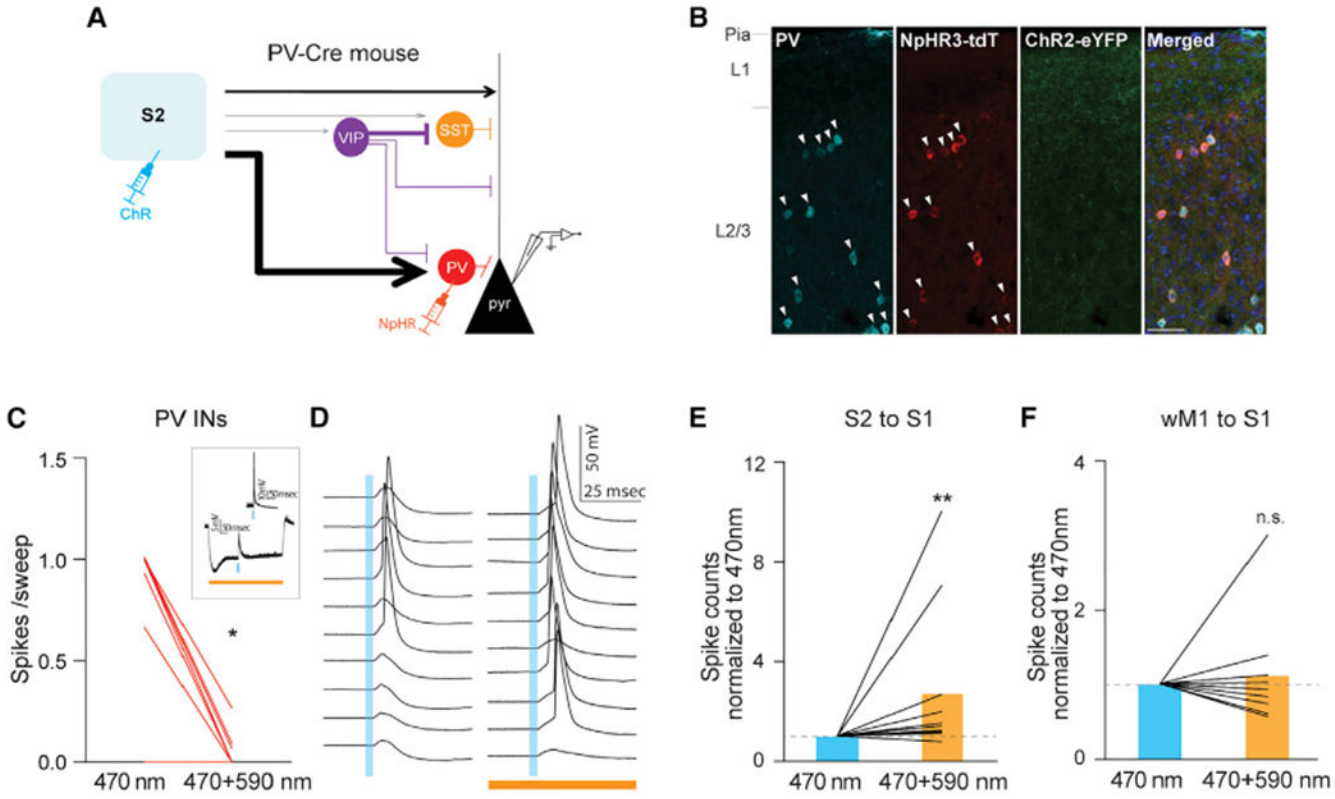

Figure 5. S2 inputs engage PV-IN-mediated feedforward inhibition of local pyramidal neurons in supragranular layers of S1

(A) Schematic of experimental design.

(B) Expression of eNpHR3.0-tdTomato was restricted to PV INs. All eNpHR3.0-tdTomato expressing neurons were PV positive (arrowhead). Scale bar, 50 μm.

(C) Photostimulation-evoked strong hyperpolarization of PV INs effectively blocked S2-driven spiking activity from PV INs. For each PV cell, averaged spikes evoked by 470 nm only or by 470 + 590 nm photostimulation were plotted (470 nm only versus 470 + 590 nm, 0.50 ± 0.13 versus 0.03 ± 0.02 spikes/sweep, 13 cells, three mice, *p = 0.0156, Wilcoxon signed-rank test). The inset shows an example of a PV cell.

(D) Photo-suppression of PV INs increased spiking probability of a Pyr neuron in response to photo-activation of S2 input. Example traces showing spiking activity of a L2/3 Pyr cell to 470 nm light only (left) and to 470 and 590 nm concurrent light stimulation (right).

(E) Population data of L2/3 Pyr cells upon S2 stimulation.

(F) wM1 inputs did not drive PV-IN-mediated feedforward inhibition of local pyramidal neuronsin supragranular layers of S1. Population data of L2/3 Pyr cells upon wM1 stimulation. Plotting conventions are same as E except photoactivation of wM1 axons instead of S2 activation. Blue bars indicate 470 nm stimulation (3 ms), orange bar indicates 590 nm (500 ms) stimulation. **p = 0.0029 (Wilcoxon signed-rank test).

See also Figure S6.

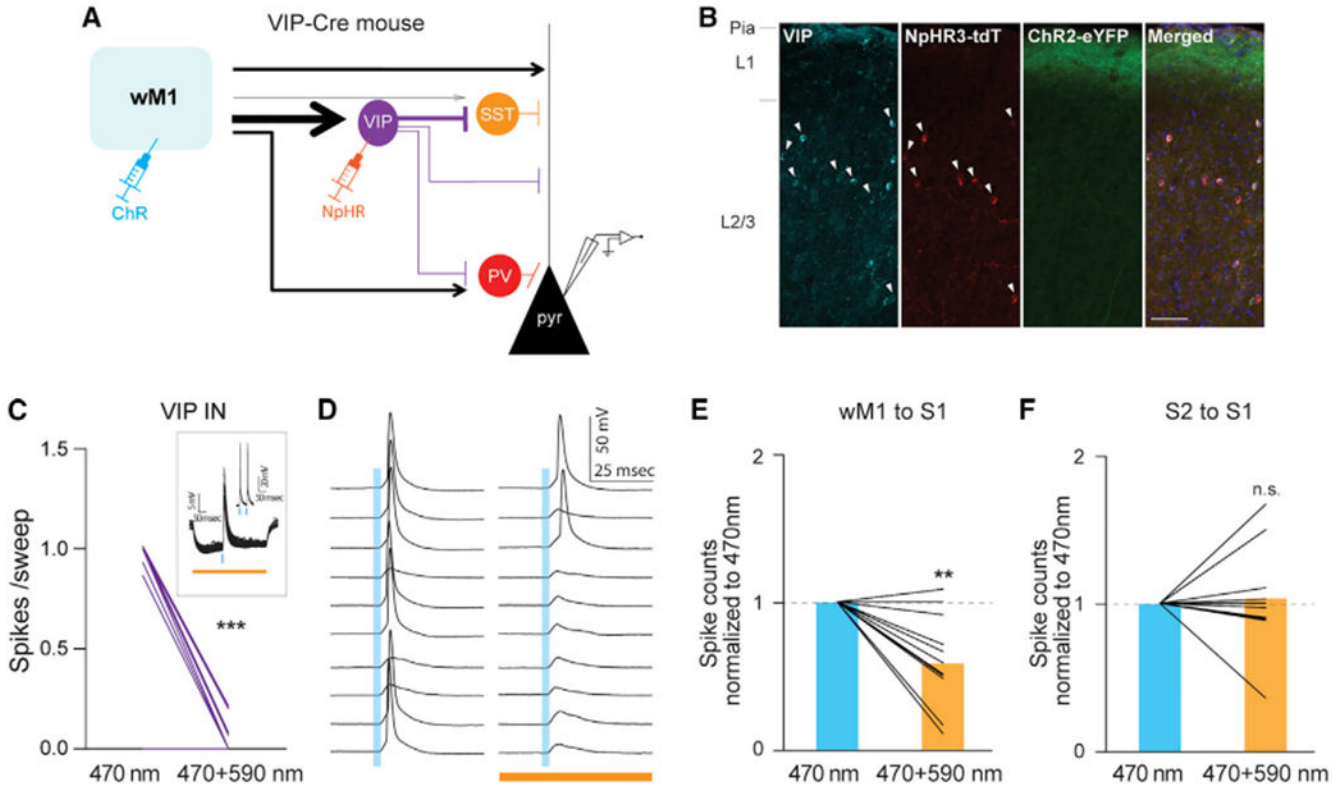

Figure 6. wM1 inputs engage VIP-IN-mediated disinhibition of local pyramidal neurons in supragranular layers of S1

(A) Schematic of experimental design.

(B) Expression of eNpHR3.0-tdTomato was restricted to VIP INs. All eNpHR3.0-tdTomato expressing neurons were VIP positive (arrowhead). Scale bar, 50 μm.

(C) Photostimulation-evoked strong hyperpolarization of VIP INs effectively block wM1-driven spiking activity from VIP INs. For each VIP cell, averaged spikes evoked by 470 nm only or 470 + 590 nm photostimulation were plotted (470 nm only versus 470 + 590 nm, 0.68 ± 0.11 versus 0.03 ± 0.01 spikes/sweep, 17 cells, four mice, ***p = 0.0005, Wilcoxon signed-rank test). The inset shows an example of a VIP cell.

(D) Photo-suppression of VIP INs increased spiking probability of a Pyr neuron in response to photo-activation of wM1 input. Example traces showing spiking activity of a layer 2/3 Pyr cell to 470 nm only (left) and to 470 and 590 nm concurrent stimulation (right).

(E) Population data of layer 2/3 Pyr cells upon wM1 stimulation.

(F) S2 inputs did not drive VIP-IN-mediated disinhibition of local pyramidal neurons in supragranular layers of S1. Population data of layer 2/3 Pyr cells upon S2 stimulation. Plotting conventions are same as (E) except photoactivation of S2 axons instead of wM1 axons. Blue bars indicate 470 nm stimulation (3 ms), orange bar indicates 590 nm (500 ms) stimulation. **p = 0.0059 (Wilcoxon signed-rank test).

See also Figure S6.

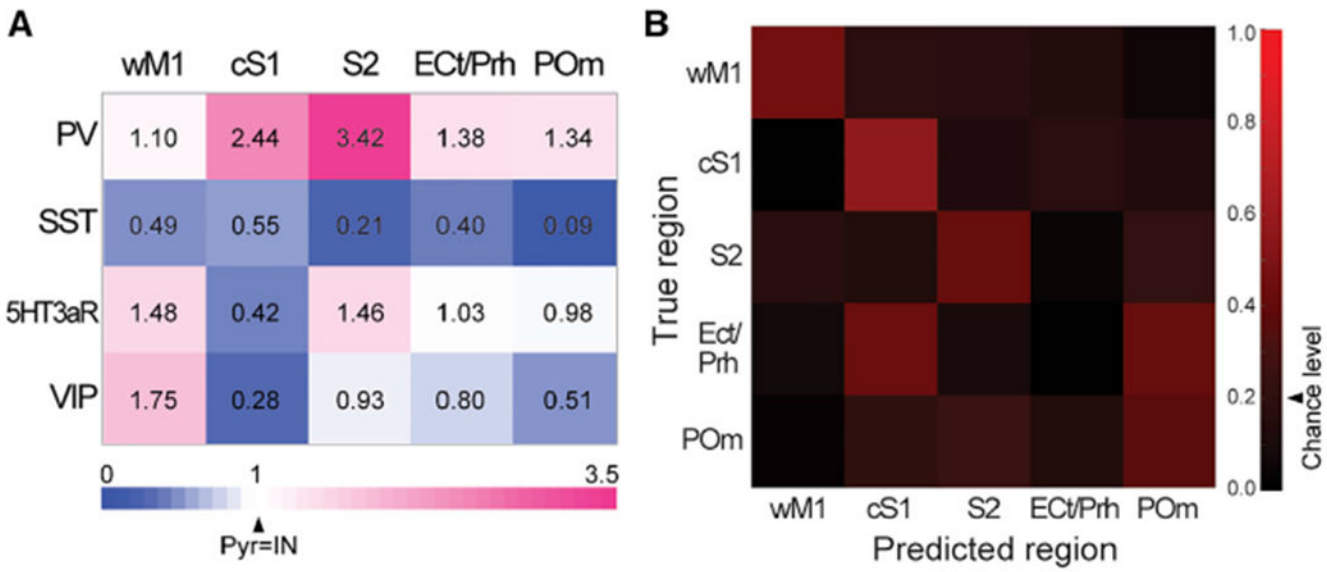

Figure 7. Characteristic combination of long-range synaptic inputs to the different types of GABAergic INs in S1

(A) Long-range input strength to each GABAergic IN subgroup for five inputs areas. Values indicate EPSCs of GABAergic INs normalized to those of simultaneously recorded nearby pyramidal neurons.

(B) Confusion matrix for multinomial regression classifier analysis. Arrowhead indicates a chance level accuracy value.

See also Figure S7.

KEY RESOURCES TABLE

REAGENT or RESOURCE	SOURCE	IDENTIFIER
Antibodies		
Rabbit anti-vasoactive intestinal peptide (VIP)	ImmunoStar	Cat. No.: 20077; RRID: AB_572270
Mouse anti-parvalbumin (PV)	Sigma-Aldrich	Cat. No.: P3088; RRID: AB_477329
AlexaFluor 647-conjugated Donkey anti-Rabbit IgG (H+L) antibody	ThermoFisher Scientific	Cat. No.: A-31573; RRID: AB_2536183
AlexaFluor 647-conjugated Donkey anti-Mouse IgG (H+L) antibody	ThermoFisher Scientific	Cat. No.: A-31571; RRID: AB_162542
AlexaFluor 488-conjugated Streptavidin	ThermoFisher Scientific	Cat. No.: S11223
AlexaFluor 546-conjugated Streptavidin	ThermoFisher Scientific	Cat. No.: S11225
Bacterial and virus strains		
AAV5.CAG.hChR2(H134R)-mCherry.WPRE.SV40	Addgene	Cat. No.: 100054-AAV5; RRID: Addgene_100054
AAV5-hSyn-hChR2(H134R)-EYFP	Addgene	Cat. No.: 26973-AAV5; RRID: Addgene_26973
AAV1-hSyn-ChETA(E123T/H134R)-eYFP-WPRE-hGH	Addgene	Cat. No.: 100049-AAV1; RRID: Addgene_100049
AAV5-Ef1a-DIO-eNpHR 3.0-EYFP	Addgene	Cat. No.: 26966-AAV5; RRID: Addgene_26966
AAV5-EF1a-DIO-eNpHR3.0-mCherry	UNC Vector Core	N/A
rAAV2-retro-CAG-Cre	NINDS Core	N/A
Chemicals, peptides, and recombinant proteins		
Tetrodotoxin (TTX)	Hello Bio	Cat. No.: HB1034
4-Aminopyridine (4-AP)	Hello Bio	Cat. No.: HB1073
Neurobiotin	Vector Laboratories	Cat. No.: SP-1120
DAPI	ThermoFisher Scientific	Cat. No.: 62247
Experimental models: organisms/strains		
Mouse: Vip-IRES-Cre	The Jackson Laboratory	JAX:010908; RRID: IMSR_JAX:010908
Mouse: Sst-IRES-Cre	The Jackson Laboratory	JAX:013044; RRID: IMSR_JAX:013044
Mouse: PV-Cre	The Jackson Laboratory	JAX:008069; RRID: IMSR_JAX:008069
Mouse: GIN	The Jackson Laboratory	JAX:003718; RRID: IMSR_JAX:003718
Mouse: Htr3a-BAC^{eGFP}	GENSAT	RRID: MMRRC_000273-UNC
Mouse: Ai9(RCL-tdT)	The Jackson Laboratory	JAX:007909; RRID: IMSR_JAX:007909
Mouse: Ai14(RCL-tdT)-D	The Jackson Laboratory	JAX:007914; RRID: IMSR_JAX:007914
Software and algorithms		
pClamp10; Clampfit 11.0.3	Molecular Devices, LLC	N/A
GraphPad Prism 9	GraphPad Software, LLC	N/A
MATLAB	MathWorks	N/A
Excel	Microsoft	N/A
ImageJ	NIH	N/A
BrainMaker	MBF Bioscience	N/A
NeuroInfo	MBF Bioscience	N/A